Simon Prato

Numerical Investigation of TEM Cells and Antenna Coupling

Master Thesis

Studies: Electrical Engineering

submitted to

Technical University of Graz

Supervisor

Dr. Thomas Bauernfeind

Graz, August 2024

Abstract

Contents

List of Figures

List of Tables

1 Introduction

2 Dipole Theory

Magnetic and electric dipoles are an effective approach for modeling the radiation of electrically small antennas. They are defined as antennas with dimensions much less than one-tenth of the wavelength ($l \ll \lambda$)[2, p. 151]. By calculating the respective dipole moments, the coupling between antennas and TEM cells can be numerically estimated. This section provides a brief introduction to the underlying theory of this concept.

Explanation Dipole Moments modeling, antennas and fields

2.1 Electric Dipoles

2.1.1 Infinitesimal Electric Dipoles

An electric dipole can be modeled as two tiny charged metal spheres or two capacitor-plates connected by a linear wire of length d and diameter a [9, p. 467], [2, p. 151]. The charges accelerate along the wire and radiate. In case of an ideal, infinitesimal dipole, the wire is very thin ($a \ll \lambda$) and very small ($d \ll \lambda$) compared to the wavelength λ [2, p. 151], [9, p. 468]. For an antenna to be accurately modeled as an infinitesimal electric dipole, its length usually must be smaller than a fiftieth of the wavelength ($d < \lambda/50$) [2, p. 156]. They are not very practical, but serve as a basic building block for more complex geometries or as a useful excitation method in numerical investigations.

An electric dipole is shown in Figure 2.1 and will now be analyzed. The dipole is aligned with the z-axis, which simplifies the mathematical calculations. Time variation according to $\mathrm{e}^{-j\omega t}$ is assumed and therefore omitted. A current flows in the wire, which is spatially uniform throughout the wire This is expressed as [2, p. 151]

$$\mathbf{I}(z) = \hat{\mathbf{a}}_z I_0. \tag{2.1}$$

The capacitances modeled at the end of the wire enable the constant current flow, which would otherwise be physically impossible. Next, the vector potential $\mathbf{A}$ is determined through the general expression

$$\mathbf{A}(\mathbf{x}) = \frac{\mu}{4\pi}\frac{\mathrm{e}^{-jkr}}{r}\iiint_V \mathbf{J}(\mathbf{x}')\,dv'. \tag{2.2}$$

The vector $\mathbf{x} = \hat{\mathbf{a}}_x x + \hat{\mathbf{a}}_y y + \hat{\mathbf{a}}_z z$ represents the observation point coordinates, while $\mathbf{x}' = \hat{\mathbf{a}}_x x' + \hat{\mathbf{a}}_y y' + \hat{\mathbf{a}}_z z'$ represents the source point coordinates. The vectors $\hat{\mathbf{a}}_x$, $\hat{\mathbf{a}}_y$, and $\hat{\mathbf{a}}_z$ are unit vectors along the x-, y-, and z-directions, respectively. $\mathbf{J}$ is the current density in the source region. The variable r is the distance from any source point to the observation point $|\mathbf{x} - \mathbf{x}'|$. In this case, the source point $\mathbf{x}' = \mathbf{0}$, due to the infinitesimal dipole [2, p. 152]. The permeability is described by μ and the propagation of the wave by e^{jkr}, where $k = 2\pi/\lambda$ is the propagation factor, or often called wavenumber.

The integration is performed over the volume V of the antenna. This leads to [2, p. 153]

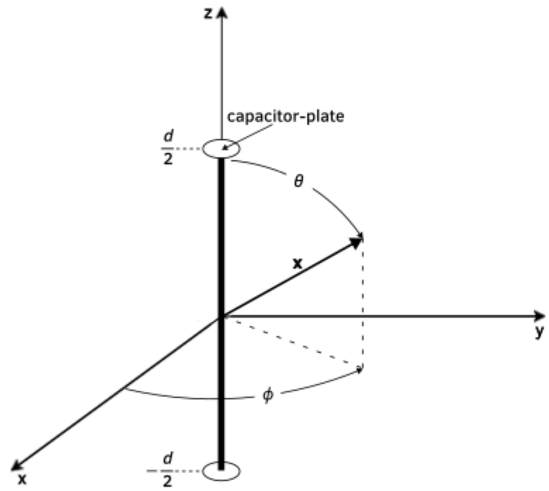

Figure 2.1 Geometrical arrangement of an infinitesimal electric dipole. It contains a capacitor-plate at each end of the wire to provide a constant current $\mathbf{I}(z)$.

$$\mathbf{A}(\mathbf{x}) = \hat{\mathbf{a}}_z \frac{\mu I_0}{4\pi r} \mathrm{e}^{-jkr} \int_{-d/2}^{+d/2} dz' = \hat{\mathbf{a}}_z \frac{\mu I_0 d}{4\pi r} \mathrm{e}^{-jkr}. \tag{2.3}$$

Any other field quantities can be derived out of the vector potential $\mathbf{A}$, such as the electric field intensity $\mathbf{E}$ and magnetic field intensity $\mathbf{H}$. To simplify this process, the Cartesian components of $\mathbf{A}$ are first transformed into spherical ones. This transform is given in matrix form as [2, p. 153]

$$\begin{bmatrix} A_r \\ A_\theta \\ A_\phi \end{bmatrix} = \begin{bmatrix} \sin\theta\cos\phi & \sin\theta\sin\phi & \cos\theta \\ \cos\theta\cos\phi & \cos\theta\sin\phi & -\sin\theta \\ -\sin\phi & \cos\phi & 0 \end{bmatrix} \begin{bmatrix} A_x \\ A_y \\ A_z \end{bmatrix}, \tag{2.4}$$

where θ is the polar angle and ϕ is the azimuthal angle of the observation point $\mathbf{x}$. $\mathbf{E}$ and $\mathbf{H}$ are then expressed by [2, p. 153],

$$\mathbf{H} = \frac{1}{\mu r} \left[\frac{\partial}{\partial r}(r A_\theta) - \frac{\partial A_r}{\partial \theta} \right] \hat{\mathbf{a}}_\phi, \tag{2.5a}$$

$$\mathbf{E} = -j\omega\mathbf{A} - j\frac{1}{\omega\mu\epsilon} \nabla\left(\nabla \cdot \mathbf{A}\right). \tag{2.5b}$$

Substituting $\mathbf{A}$ into Equations (2.5a) and (2.5b) reduces them to

$$E_r = \eta \frac{I_0 d \cos\theta}{2\pi r^2} \left[1 + \frac{1}{jkr} \right] \mathrm{e}^{-jkr}, \tag{2.6a}$$

$$E_\theta = j\eta \frac{kI_0 d \sin\theta}{4\pi r}\left[1 + \frac{1}{jkr} - \frac{1}{(kr)^2}\right]\mathrm{e}^{-jkr}, \tag{2.6b}$$

$$E_\phi = 0. \tag{2.6c}$$

and,

$$H_r = H_\theta = 0, \tag{2.7a}$$

$$H_\phi = j\frac{kI_0 d \sin\theta}{4\pi r}\left[1 + \frac{1}{jkr}\right]\mathrm{e}^{-jkr}, \tag{2.7b}$$

$\eta = \sqrt{\frac{\mu}{\epsilon}}$ is the wave impedance of the medium in which the waves travel.

The total radiated power of the dipole is obtained by integrating the complex Poynting vector $\mathbf{W}$ over a closed surface surrounding the dipole [2, p. 154]. The real part of the total radiated power provides information about energy transferred by radiation, while the imaginary part about the antenna's reactive behavior. $\mathbf{W}$ is defined by

$$\mathbf{W} = \frac{1}{2}\left(\mathbf{E} \times \mathbf{H}^*\right). \tag{2.8}$$

The real power transfer is derived through the time-averaged Poynting vector $\mathbf{W}_{\mathrm{av}}$ [2, p. 160], which is calculated by

$$\mathbf{W}_{\mathrm{av}} = \frac{1}{2}\Re\{\mathbf{E} \times \mathbf{H}^*\}. \tag{2.9}$$

The complex power P is derived by integrating $\mathbf{W}$ over a closed surface around the dipole, which leads to [2, p. 154]

$$P_r = \eta\frac{\pi}{3}\frac{|I_0 l|^2}{\lambda}\left[1 - j\frac{1}{(kr)^3}\right]. \tag{2.10}$$

Equation 2.10 demonstrates, that the imaginary part of the power radiated by the infinitesimal electric dipole shows capacitive behavior.

2.1.2 Small Electric Dipoles

Wires that are too long to be modeled as an infinitesimal dipole, but short enough to be considered electrically small ($\lambda/50 < l \leq \lambda/10$), are classified as small physical dipoles [2, pp. 162-163]. They are a more accurate and useful representation of a linear wire antenna, and now investigated further.

A current I_0 is fed into the short, center-fed, linear antenna shown in Figure 2.1. The current along the antenna arms $I(z)$ linearly drops to zero [12, p. 412], as visualized in Figure 2.3. Mathematically, it is described by,

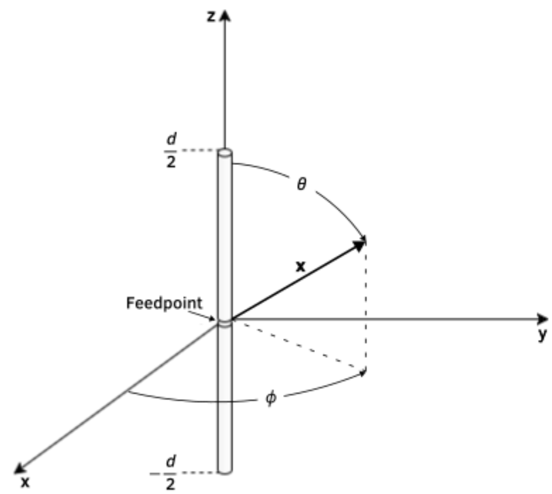

Figure 2.2 Geometrical arrangement of a linear, center-fed wire antenna with a feedpoint indicated in the center. The feedpoint consists of a small gap providing current I_0 to the antenna.

$$\mathbf{I}(z) = \hat{\mathbf{a}}_z I_0 \left(1 - \frac{2|z|}{d}\right). \tag{2.11}$$

This is different to the current distribution of the infinitesimal dipole. The capacitor-plates are therefore not needed in this model. Furthermore, charge accumulates along the antenna due to the linear drop of current $\mathbf{I}$. It is expressed as a charge per unit length ρ', which is appropriate due to the thin wire. It is derived by the continuity equation $j\omega\rho = \nabla \cdot \mathbf{J}$, which leads to [12, pp. 410-412]

$$\rho' = \pm \frac{\mathrm{d}}{\mathrm{d}z} j \frac{I(z)}{\omega} = \pm j \frac{2I_0}{\omega d}. \tag{2.12}$$

ρ' is uniformly distributed along each antenna arm.

An important metric is the electric dipole moment $\mathbf{p}$. It is defined as the product of charge density ρ along the antenna and their source point $\mathbf{x}'$ [12, p.410], and generally expressed as

$$\mathbf{p} = \iiint_V \mathbf{x}' \rho(\mathbf{x}')\, dv'. \tag{2.13}$$

The charge distribution ρ' enables the calculation of the electric dipole moment $\mathbf{p}$, which results in

$$\mathbf{p} = \int_{-\frac{d}{2}}^{\frac{d}{2}} z\rho'(z)\, dz \cdot \hat{\mathbf{a}}_z = j \frac{I_0 d}{2\omega} \cdot \hat{\mathbf{a}}_z. \tag{2.14}$$

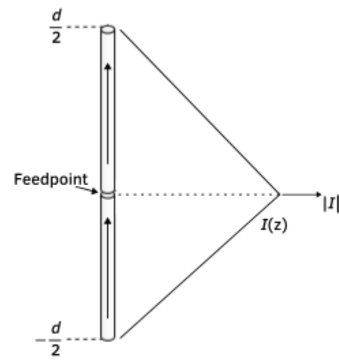

Figure 2.3 Current distribution across linear wire antenna. It has a maximum at the feedpoint, and drops to zero at points $d/2$ and $-d/2$.

The electric dipole moment $\mathbf{p}$ is parallel to the antenna's arms and points in the z-direction [12, p. 412], [9, p. 155]. Next, the vector potential $\mathbf{A}$ is determined using Equation 2.2. The calculations of $\mathbf{A}$ simplify to [12, p. 410],

$$\mathbf{A}(\mathbf{x}) = -j\frac{\mu\omega}{4\pi}\mathbf{p}\frac{\mathrm{e}^{-jkr}}{r} \tag{2.15}$$

The formulation of $\mathbf{A}$ now contains an additional factor of $1/2$, compared to the previously derived $\mathbf{A}$ of the infinitesimal dipoles in Equation 2.3. This is due to the integration process of $\mathbf{I}$. When integrated over the same interval $[-d/2, d/2]$, the linearly dropping $\mathbf{I}$ yields half the value of a constant $\mathbf{I}$. Furthermore, it makes sense to keep $\mathbf{x'} = \mathbf{0}$ for simplicity reasons. It has been shown, that this approximation is sufficient for large r, and the amplitude error remains negligible for small r [12, p. 409], [2, pp. 164-168].

This makes it reasonable to model electrically small antennas with infinitesimal dipoles

The short physical electric dipole described in this section approximate the behavior of electrically short antennas. Special care must be taken of the excitation method and shape, as it influences the behavior [12, p. 413]. Additionally, any antenna investigated through this method must remain as small as possible compared to the wavelength λ, to reduce any analytical approximation errors.

Image theory may be added for TEM cell explanations [**Balanis**]

2.2 Magnetic Dipoles

The magnetic dipole moment characterizes the strength of a magnetic source. A small current loop fed with a current I_0 can be used to model the magnetic dipole, as demonstrated in Figure 2.4. This relation holds as long as its overall length is smaller than a tenth of the wavelength ($2b\pi < \lambda/10$) and as long as the the wire is very thin [2, p. 231]. Furthermore, the radiation pattern of the magnetic dipole is equal to that of the electric dipole, with the role of the electric and magnetic fields interchanged [9, p. 254].

The magnetic dipole moment $\mathbf{m}$ is given by [12, p. 413]

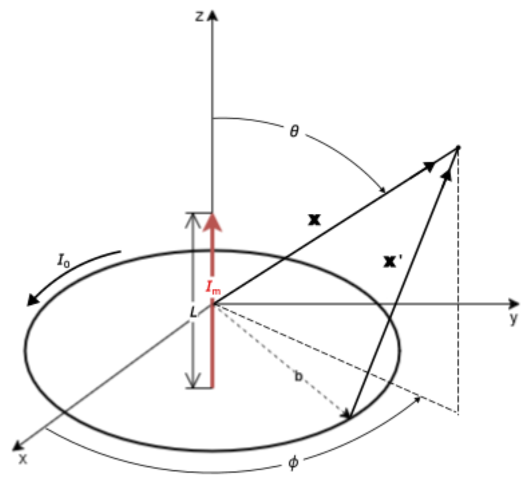

Figure 2.4 Geometrical arrangement of a current loop fed by a current I_0, producing a magnetic dipole moment. Alternatively, a magnetic current I_m flows perpendicular to the loop's area along the distance L, which produces an equivalent magnetic dipole moment.

$$\mathbf{m} = \frac{1}{2} \iiint_V (\mathbf{x}' \times \mathbf{J})\, dv'. \tag{2.16}$$

Furthermore, the magnetic current I_m and the electric current I_0 in the loop are related with [2, p. 237]

$$I_m L = jA\omega\mu_0 I_0 \tag{2.17}$$

with $A = b^2\pi$ being the area of the current loop. Analogous to the separation distance d in the electric dipole, L is the length of the magnetic dipole. I_m and L may be used to model the magnetic dipole moment instead of the current loop. The fields **E** and **H** generated are the same in both cases. This means, that the infinitesimal magnetic dipole can be replaced with an electrically small loop [2, p. 237]. This was not the case for the infinitesimal and electrically small electric dipoles. **E** and **H** of the magnetic dipole moment or electrically small current loop are then determined with [2, p. 237]

$$E_r = E_\theta = 0, \tag{2.18a}$$

$$E_\phi = -j\frac{kI_m d\sin\theta}{4\pi r}\left[1 + \frac{1}{jkr}\right]\mathrm{e}^{-jkr}, \tag{2.18b}$$

and,

$$H_r = \frac{I_m d\cos\theta}{2\pi r^2\eta}\left[1 + \frac{1}{jkr}\right]\mathrm{e}^{-jkr}, \tag{2.19a}$$

$$H_\theta = j\frac{kI_m d\sin\theta}{4\pi r\eta}\left[1+\frac{1}{jkr}-\frac{1}{(kr)^2}\right]\mathrm{e}^{-jkr}, \tag{2.19b}$$

$$H_\phi = 0. \tag{2.19c}$$

The complex power density **W** can be derived analogous to the the electric dipole case in Equation 2.8. For the magnetic dipole, the imaginary part of **W** has the opposite sign compared to the electric dipole. This is the result of the near-field power being inductive in case of the magnetic dipole, while it is capacitive for the electric dipole. The complex power equals to

$$P_r = \eta\left(\frac{\pi}{12}\right)(ka)^4|I_0|^2\left[1+j\frac{1}{(kr)^3}\right], \tag{2.20}$$

and its imaginary part is inductive [2, p. 238].

2.3 Crossed Dipoles

Section todo

Crossed dipoles can generate a wide variety of radiation patterns. Supposed two dipoles are placed perpendicular to each other and fed 90° out of phase, an omnidirectional radiation pattern in created [26]. If the equivalent dipoles of an EUT represents such two dipoles, any mode which can propagate in the TEM cell will do so, and therefore influence the measurement result. It is therefore not only important to know which dipoles there are representing the EUT, but also what phase and magnitude they have. Meaning that not only the dipoles aligned with the TEM mode alone influence the result.

Dipoles next to conducting planes (balanis, collin)

2.4 Radiated Field

2.4.1 Field regions

The field quantities **E** and **H** have been derived for an infinitesimal electric dipole in Equations (2.6a) to (2.6c) and Equations (2.7a) and (2.7b), and for an infinitesimal magnetic dipole in Equations (2.19a) to (2.19c) and Equations (2.18a) and (2.18b). They are valid everywhere except for the source region [2, p. 156].

Depending on the distance r to the dipole, the behavior of the fields changes. This becomes apparent when investigating the expressions $1/(jkr)$ and $1/(kr)^2$ in Equations (2.6a) to (2.6c) and Equations (2.7a) and (2.7b) of the infinitesimal electric dipole. These expressions are highlighted here in the case of E_θ, although they partly also appear in E_r and H_ϕ, and referred to as Expression 1 and Expression 2 in

$$E_\theta = j\eta\frac{kI_0 d\sin\theta}{4\pi r}\left[1+\underbrace{\frac{1}{jkr}}_{\text{Expression 1}}-\underbrace{\frac{1}{(kr)^2}}_{\text{Expression 2}}\right]\mathrm{e}^{-jkr}. \tag{2.21}$$

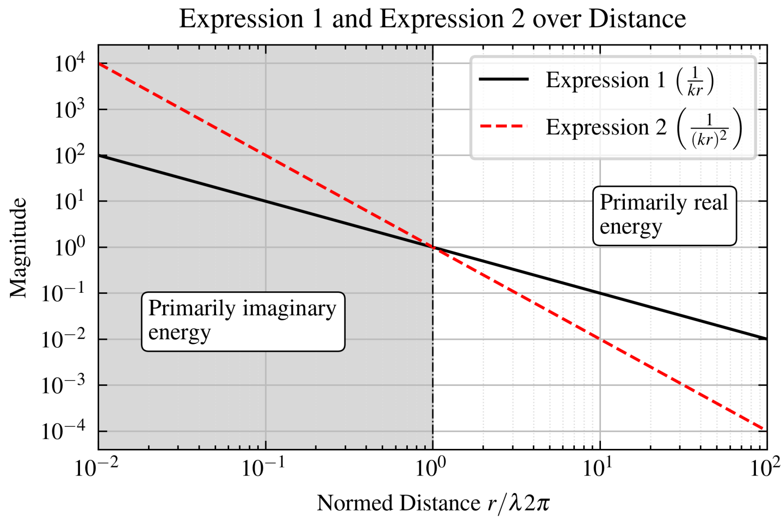

Figure 2.5 Behavior of Expression 1 and Expression 2 in Equation 2.21 over distance r. The distance r is normalized to the radian distance $\lambda/2\pi$. The magnitude of both expressions is normed to 1 at radian distance for better comparison.

If the distance $r < \lambda/2\pi$ ($kr < 1$), then Expression 2 delivers the largest value in the brackets. Consequently, the energy stored in this region is mostly imaginary, especially if $r \ll \lambda/\pi$ ($kr \ll 1$). It is referred to as the near-field region.

At distances $r > \lambda/2\pi$ ($kr > 1$), Expression 1 exceeds Expression 2 in value. The real part of the energy is larger than the imaginary part. This region is referred to as the intermediate-field region. For $r \gg \lambda/2\pi$ ($kr \gg 1$) the energy is primarily real, indicating radiation. This region is called the far-field region.

At $r = \lambda/2\pi$ ($kr = 1$), Expression 1 and Expression 2 are of equal magnitude. This is marked as the radian distance [2, pp. 156-160]. The radian distance therefore represents an important transition point between field regions, where the behavior of the fields shifts. Figure 2.5 visualizes Expression 1 and Expression 2 over r. The same analysis of the field region is also valid for the infinitesimal magnetic dipole.

Antennas, which cannot be modeled as infinitesimal dipoles, such as the linear wire antenna, are surrounded by different field regions. They are shown in Figure 2.6. The far-field region contains mostly real energy, and the antenna may be most accurately approximated by an infinitesimal electric dipole. In the radiating near-field, the energy is largely real, but depends on the distance r. Lastly, in the reactive near-field the energy is mostly imaginary.

The far-field region starts at approximately r_2 and the radiating near-field at r_1, which are defined as

$$r_1 = 0.62\sqrt{d^3/\lambda}, \tag{2.22a}$$

$$r_2 = 2d^2/\lambda. \tag{2.22b}$$

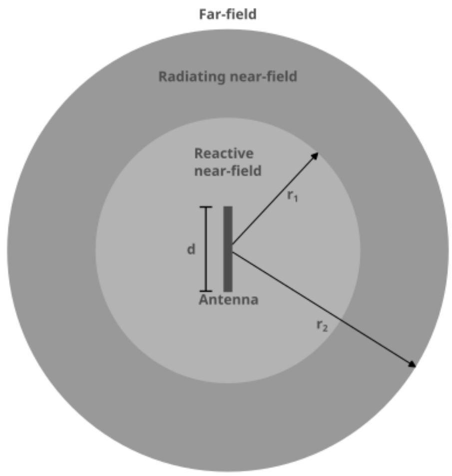

Figure 2.6 Field regions of an antenna, here specifically a linear wire antenna. However, they are applicable for any antenna, as long as their largest dimension d is known.

Here, d is the largest dimension of the antenna. In the case of the linear wire antenna, d is the wire length [2, pp. 165-170].

2.4.2 Energy densities and reactances

The energy density is given by [9, p. 330]

$$w_{\mathrm{EM}} = \frac{1}{2}\left(\underbrace{\epsilon E^2}_{\text{Electric energy} w_E} + \underbrace{\frac{1}{\mu}B^2}_{\text{Magnetic energy} w_M}\right). \tag{2.23}$$

Integrating w_{EM} over a volume yields the total electromagnetic energy in this volume. Similarly, integrating w_E gives the electric energy in said volume, and w_M the magnetic energy.

If all of the energy is provided by an electrically short antenna, its equivalent reactances can be derived through [9, pp 107, 328]

$$L = 2\frac{W_m}{I^2} \tag{2.24a}$$

$$C = 2\frac{W_e}{V^2} \tag{2.24b}$$

3 Guided Waves

3.1 Lorentz Reciprocity Theorem

The Lorentz reciprocity theorem proves to be very useful for further analysis. Let two source pairs $\mathbf{J_1}$, $\mathbf{M_1}$ and $\mathbf{J_2}$, $\mathbf{M_2}$ exist in a volume V, bounded by the closed surface S.

The medium in V is linear and isotropic. The source pairs generate fields $\mathbf{E_1}$, $\mathbf{H_1}$ and $\mathbf{E_2}$, $\mathbf{H_2}$, respectively, with the same frequency. The fields and source pairs can then be related with [2, p. 145], [7, p. 49]

$$-\nabla \cdot (\mathbf{E}_1 \times \mathbf{H}_2 - \mathbf{E}_2 \times \mathbf{H}_1) = \mathbf{E}_1 \cdot \mathbf{J}_2 + \mathbf{H}_2 \cdot \mathbf{M}_1 - \mathbf{E}_2 \cdot \mathbf{J}_1 - \mathbf{H}_1 \cdot \mathbf{M}_2. \tag{3.1}$$

Integrating Equation 3.1 over V, and converting the volume integral to a surface integral with the divergence theorem, leads to [2, p. 145], [7, p. 50]

$$\begin{aligned} &-\oiint_S (\mathbf{E}_1 \times \mathbf{H}_2 - \mathbf{E}_2 \times \mathbf{H}_1) \cdot d\mathbf{s}' \\ &\qquad = \iiint_V (\mathbf{E}_1 \cdot \mathbf{J}_2 + \mathbf{H}_2 \cdot \mathbf{M}_1 - \mathbf{E}_2 \cdot \mathbf{J}_1 - \mathbf{H}_1 \cdot \mathbf{M}_2) \cdot dv'. \end{aligned} \tag{3.2}$$

This is a very useful integral equation, which relates the coupling of different source points. If one of these sources is set to zero, they can serve as observation points. This can be done to investigate, for example, modes and their coupling in a waveguide. Suppose the volume V does not contain sources $\mathbf{J}_1 = \mathbf{M}_1 = \mathbf{J}_2 = \mathbf{M}_2 = \mathbf{0}$. Then, the Lorentz Reciprocity theorem in differential and integral form would be [2, pp. 145-146]

$$\nabla \cdot (\mathbf{E}_1 \times \mathbf{H}_2 - \mathbf{E}_2 \times \mathbf{H}_1), \tag{3.3a}$$

$$\oiint_S (\mathbf{E}_1 \times \mathbf{H}_2 - \mathbf{E}_2 \times \mathbf{H}_1) \cdot d\mathbf{s}' = 0, \tag{3.3b}$$

which the modes in the waveguide must fulfill.

There could be a sketch made with such a waveguide an H1, E1, H2, E2

Another application arises when investigating a volume V confined by a perfectly conducting surface S, in which the linear current densities $\mathbf{J}_1$ and $\mathbf{J}_2$ flow. Because $\mathbf{n} \times \mathbf{E}_1 = \mathbf{n} \times \mathbf{E}_2 = 0$ along the surface S, the surface integral in Equation 3.2 vanishes, and

$$\mathbf{E}_1 \cdot \mathbf{J}_2 = \mathbf{E}_2 \cdot \mathbf{J}_1, \tag{3.4}$$

arise. This is the Rayleigh-Carson form of the Lorentz reciprocity theorem. It states that $\mathbf{J}_1$ generates $\mathbf{E}_1$, which has components along $\mathbf{J}_2$, that are equal to the same components of $\mathbf{E}_2$ along $\mathbf{J}_1$, and vice versa [7, p. 50].

Concluding, the Lorentz Reciprocity theorem is useful to derive reciprocal aspects of waveguides, finding orthogonal properties of modes, investigating fields generated by currents and dipole moments in waveguides [7, p. 50], and much more. It will serve in the remainder of this thesis.

3.2 Green's Function

3.2.1 Scalar Green's Function

The Green's function describes the response of a linear differential operator L to a point source of unit strength. It is explained briefly in the following with an example of solving the Poisson's equation with boundary conditions, since this concept will be used in further analysis. The general form for a Green's function of a given problem is

$$LG(\mathbf{x}, \mathbf{x}') = -\delta(\mathbf{x} - \mathbf{x}'). \tag{3.5}$$

A point source of unit strength is generally modeled with a delta function δ at a certain point in one-dimensional space. In multi-dimensional space, a product of delta-functions are used.

Once Equation 3.5 is solved for a point source of unit strength, and the Green's function G of this specific problem is known, it can be used to for any combination of point sources f to solve for an input function u,

$$Lu(\mathbf{x}) = f(\mathbf{x}), \tag{3.6}$$

This is done through superposition through point sources of unit strength, as in

$$u(\mathbf{x}) = \iiint_V G(\mathbf{x}, \mathbf{x}')f(\mathbf{x}')dv'. \tag{3.7}$$

The integrands are the source point variables x', y', z'.

One application of the Green's function is solving the Poisson's equation. The scalar potential ϕ can be calculated from a density of charge distribution ρ by using the Green's function of this specific problem. If there are no boundaries present, it takes the form

$$\nabla^2 \phi = -\frac{\rho}{\epsilon}, \tag{3.8a}$$

$$\phi(\mathbf{x}) = \frac{1}{4\pi\epsilon} \iiint_V \frac{\rho(\mathbf{x}')}{|\mathbf{x} - \mathbf{x}'|} dv', \tag{3.8b}$$

where ϵ is the permittivity of the medium.

The Green's function for this problem equals $G(\mathbf{x}, \mathbf{x}') = \frac{1}{4\pi|\mathbf{x}-\mathbf{x}'|}$, and represents the potential at position $\mathbf{x}$ created by an unit point charge at point $\mathbf{x}'$. In this case, the input function $u = \phi$ and the source function $f = -\rho/\epsilon_0$.

Different volumes of interest V_1, V_2, ..., V_n can be connected by applying boundary conditions on their surrounding surfaces S_1, S_2, ..., S_n. Applying Green's second identity on the Poisson's equation enables enforcing such a boundary condition upon the surrounding surface S of a volume V,

This will become useful for the greens function in tem cell: Perturbed

$$\iiint_V \left(\phi\nabla^2_{\mathbf{x}'}G - G\nabla^2_{\mathbf{x}'}\phi\right) dv' = \oiint_S \left(G\frac{\partial\phi}{\partial\mathbf{n}} - \phi\frac{\partial G}{\partial\mathbf{n}}\right) d\mathbf{s}'. \tag{3.9}$$

The vector $\mathbf{n}$ is normal to S. The operator $\nabla^2_{\mathbf{x}'}$ differentiates with respect to the source vector $\mathbf{x}'$ due to x', y', z' being the integrands. Inserting $\nabla^2\phi = -\rho/\epsilon$ from Equation 3.8a and $\nabla^2 G = -\delta$ from Equation 3.5 leads to

$$\phi = \frac{1}{\epsilon}\iiint_V \rho(\mathbf{x}')G(\mathbf{x},\mathbf{x}')\cdot dv' + \oiint_S \left(\phi\frac{\partial G}{\partial\mathbf{n}} - G\frac{\partial\phi}{\partial\mathbf{n}}\right) d\mathbf{s}' \tag{3.10}$$

ϕ or its normal derivative to the surface $\partial\phi/\partial\mathbf{n}$ can be forced on the boundary. If only one of those two expressions is known on the boundary surface, the Green's function may be modified such that the unknown expression vanishes. If ϕ is defined on the whole boundary, it satisfies Dirichlet boundary conditions. On the other hand, if $\partial\phi/\partial\mathbf{n}$ is defined on the whole boundary, it satisfies Neumann boundary conditions [7, pp. 55-59].

3.2.2 Dyadic Green's Function

While the scalar Green's function is useful for solving one-dimensional differential equations, the dyadic Green's function $\bar{\mathbf{G}}$ is more suitable for three-dimensional problems. It relates a vector source with a vector response, which is necessary when solving the vector Helmholtz equation in

$$\nabla^2\mathbf{A} + k^2\mathbf{A} = -\mu\mathbf{J}. \tag{3.11}$$

When replacing $\mu\mathbf{J}$ by an unit vector source $(\hat{\mathbf{a}}_x + \hat{\mathbf{a}}_y + \hat{\mathbf{a}}_z)\,\delta(\mathbf{x}-\mathbf{x}')$, the solution for $\mathbf{A}$ of Equation 3.11 in free-space is

$$(\hat{\mathbf{a}}_x + \hat{\mathbf{a}}_y + \hat{\mathbf{a}}_z)\frac{e^{-jk|\mathbf{x}-\mathbf{x}'|}}{4\pi|\mathbf{x}-\mathbf{x}'|}. \tag{3.12}$$

This is a vector Green's Function by definition [7, pp. 91-92].

Each component of the current distribution $\mathbf{J}$ generates fields through a linear relation. This relationship can effectively be represented by dyadics, which are linear mappings between vectors. The dyadic Green's function is therefore introduced and defined as

$$\begin{aligned}\bar{\mathbf{G}} =& G_{xx}\,\hat{\mathbf{a}}_x\hat{\mathbf{a}}_x + G_{xy}\,\hat{\mathbf{a}}_x\hat{\mathbf{a}}_y + G_{xz}\,\hat{\mathbf{a}}_x\hat{\mathbf{a}}_z + \\ & G_{yx}\,\hat{\mathbf{a}}_y\hat{\mathbf{a}}_x + G_{yy}\,\hat{\mathbf{a}}_y\hat{\mathbf{a}}_y + G_{yz}\,\hat{\mathbf{a}}_y\hat{\mathbf{a}}_z + \\ & G_{zx}\,\hat{\mathbf{a}}_z\hat{\mathbf{a}}_x + G_{zy}\,\hat{\mathbf{a}}_z\hat{\mathbf{a}}_y + G_{zz}\,\hat{\mathbf{a}}_z\hat{\mathbf{a}}_z\end{aligned}$$

Each component of the current vector $\mathbf{J}$ is associated with one unit vector of the Green's function, i.e. J_x with $\hat{\mathbf{a}}_\mathbf{x}$, J_y with $\hat{\mathbf{a}}_\mathbf{y}$ and J_z with $\hat{\mathbf{a}}_\mathbf{z}$ [7, p. 92]. Consequently, the field generated by a current component in a given direction is determined by the corresponding column of the dyadic Green's function. For example, if only a current component J_x is present, the field components A_x, A_y, and A_z are obtained from the Green's functions elements G_{xx}, G_{yx} and G_{zx}.

The dyadic Green's function is defined as the solution of

$$\nabla^2 \bar{\mathbf{G}}(\mathbf{x}, \mathbf{x}') + k^2 \bar{\mathbf{G}} = -\bar{\mathbf{I}}\delta(\mathbf{x} - \mathbf{x}'). \tag{3.13}$$

In free space, a commonly used form of the dyadic Green's function is given by [7, p.92]

$$\bar{\mathbf{G}}(\mathbf{x}, \mathbf{x}') = \bar{\mathbf{I}} \frac{e^{-jk|\mathbf{x}-\mathbf{x}'|}}{4\pi|\mathbf{x} - \mathbf{x}'|}, \tag{3.14}$$

where $\bar{\mathbf{I}}$ is an unit dyadic. The free-space case is presented here to provide an overview. Dyadic Green's functions can also be derived for bounded geometries, such as waveguides, by implementing appropriate boundary conditions.

The fields $\mathbf{A}$ generated by arbitrary $\mathbf{J}$ can be expressed with the dyadic Green's function as

$$\mathbf{A}(\mathbf{x}) = \mu \iiint_V \bar{\mathbf{G}} \left(\mathbf{x}, \mathbf{x}'\right) \mathbf{J}(\mathbf{x}') \, dv'. \tag{3.15}$$

Each component of $\mathbf{J}$ drives a combination of components in $\mathbf{A}$. Dyadics capture this component-wise coupling and simplify the notation [7, p. 92].

Note: Chapter is called "Guided Waves", but this chapter presents free-space solutions

The dyadic Green's Function is commonly applied to calculate field distributions in waveguides. In [29] it is used to derive the fields in a TEM cell caused by a vertical current conducting wire with help of the small-gap approximation.

3.3 Modes in Waveguides

3.3.1 Rectangular Waveguides as non-TEM structures

A hollow rectangular waveguide with perfectly conducting walls cannot support TEM modes. This can be shown directly from Maxwell's equation, as done in [9, pp. 425-427]. The first two dominant modes are demonstrated in Figure 3.1. The electric field intensity $\mathbf{E}$ and magnetic field intensity $\mathbf{H}$ are defined as

$$\mathbf{E} = (E_{0,x} \cdot \hat{\mathbf{a}}_x + E_{0,y} \cdot \hat{\mathbf{a}}_y + E_{0,z} \cdot \hat{\mathbf{a}}_z)\mathrm{e}^{-jkz}, \tag{3.16a}$$

$$\mathbf{H} = (H_{0,x} \cdot \hat{\mathbf{a}}_x + H_{0,y} \cdot \hat{\mathbf{a}}_y + H_{0,z} \cdot \hat{\mathbf{a}}_z)\mathrm{e}^{-jkz}. \tag{3.16b}$$

Using Faraday's and Ampère-Maxwell law transforms Equations (3.16a) to (3.16b) to

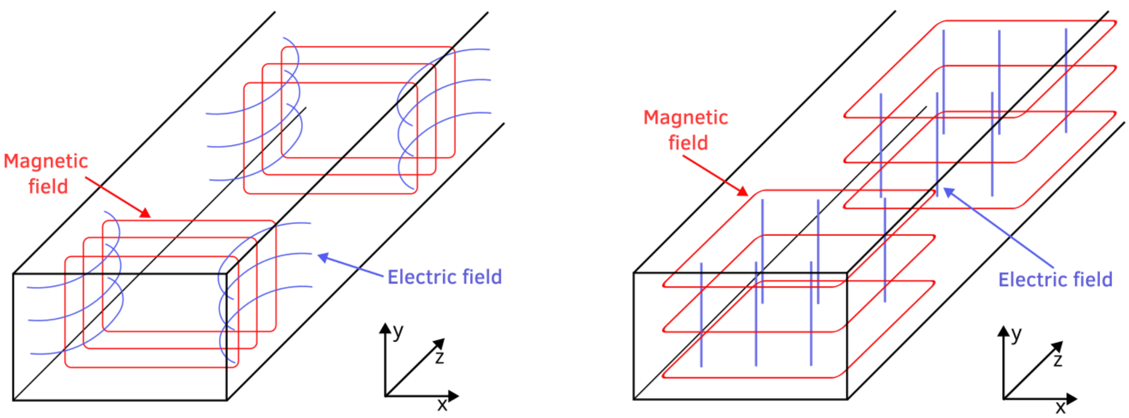

(a) TM_{11} mode

(b) TE_{10} mode

Figure 3.1 Dominant modes in a rectangular waveguide.

$$\nabla \times \mathbf{E} = \begin{pmatrix} \frac{\mathrm{d}}{\mathrm{d}y} E_z - \mathrm{i}k E_y \\ \mathrm{i}k E_x - \frac{\mathrm{d}}{\mathrm{d}x} E_z \\ \frac{\mathrm{d}}{\mathrm{d}x} E_y - \frac{\mathrm{d}}{\mathrm{d}y} E_x \end{pmatrix} = \begin{pmatrix} -\mathrm{i}\omega B_x \\ -\mathrm{i}\omega B_y \\ -\mathrm{i}\omega B_z \end{pmatrix}, \tag{3.17a}$$

$$\nabla \times \mathbf{B} = \begin{pmatrix} \frac{\mathrm{d}}{\mathrm{d}y} B_z - \mathrm{i}k B_y \\ \mathrm{i}k B_x - \frac{\mathrm{d}}{\mathrm{d}x} B_z \\ \frac{\mathrm{d}}{\mathrm{d}x} B_y - \frac{\mathrm{d}}{\mathrm{d}y} B_x \end{pmatrix} = \begin{pmatrix} \frac{\mathrm{i}\omega}{\mu\epsilon} E_x \\ \frac{\mathrm{i}\omega}{\mu\epsilon} E_y \\ \frac{\mathrm{i}\omega}{\mu\epsilon} E_z \end{pmatrix}. \tag{3.17b}$$

For a TEM mode, the longitudinal field components vanish $E_\mathrm{z} = H_\mathrm{z} = 0$. Under this assumption, Equations (3.17a) to (3.17b) together with the Gauss' law and Faraday's law reduce to the following conditions for $\mathbf{E}$ components:

$$\frac{\mathrm{d}}{\mathrm{d}x} E_x + \frac{\mathrm{d}}{\mathrm{d}y} E_y = 0 \quad \text{Derived out of Gauss' law,} \tag{3.18}$$

$$\frac{\mathrm{d}}{\mathrm{d}y} E_x - \frac{\mathrm{d}}{\mathrm{d}x} E_y = 0 \quad \text{Derived out of Faraday's law.} \tag{3.19}$$

The derived Equations (3.18) to (3.19) cannot fulfill any boundary conditions imposed by the rectangular waveguide. Therefore, a TEM mode cannot propagate.

3.3.2 TEM mode in the TEM cell

TODO: Unvollendetes Kapitel. Es soll die Ausbreitung des TEM Modes in der TEM Zelle durch [27, 29] erklärt werden.

Opposed to the rectangular waveguide, a TEM cell conducts TEM waves. The TEM mode is necessarily excited by the geometry of the TEM cell, hence this mode is called essential.

The higher order TE and TM modes, which are only excited due to non-uniformity of the TEM cell, are called non-essential modes [13].

A TEM cell solves this problem, by having a gap between the septum and the side walls. Essentially, it can be considered as two rectangular waveguides with apertures on the sides. Those apertures allow perturbations of the electromagnetic fields between them. The boundary conditions of the Laplace equation now changed due to the gaps. The Green's function may be calculated of the new construction, now considering the boundary conditions at the gaps, which must be the same for both waveguides (to prevent discontinuities). In the papers of Tippet, Chang and Wilson, this new Green's function lead to the excitation of TEM modes in both waveguides [27, 29]. However, the gap is assumed to be small, electrically ($\xi g \ll 1$) and compared to the septum width ($g/a \ll 1$) [30]. The variable $\xi = \sqrt{k_0^2 - \beta^2}$ is the transverse (in y-direction) propagation constant, and consists of the free-space wave number k_0 and longitudinal (in z-direction) propagation constant β. The variables g and a are geometry variables of the TEM cell annotated in Figure 3.2.

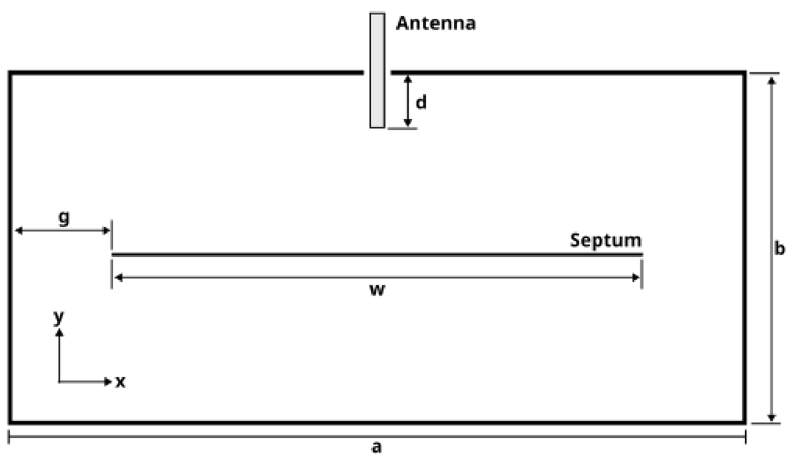

Figure 3.2 TEM cell with vertical antenna inserted

3.3.3 Higher-order modes

The TEM cell under investigation has a width of $a = 40\,\mathrm{mm}$ and a height of $b = 24\,\mathrm{mm}$. A cross section of the TEM cell with the important dimensions is shown in Figure 3.3. For a thin septum ($t/b \ll 0.1$), the cut-off frequency f_c of modes with n-even subscripts, i.e. $\mathrm{TE}_{\mathrm{m,2n}}$ and $\mathrm{TM}_{\mathrm{m,2n}}$ modes, is approximated as

$$f_c = \frac{c}{2}\sqrt{\left(\frac{m}{a}\right)^2 + \left(\frac{n}{b}\right)^2}. \tag{3.20}$$

- f_c: cutoff frequency of the mode T_{mn}
- c: speed of light in the medium (approximately $3 \times 10^8\,\mathrm{m/s}$ in air)
- a: wider dimension (broad wall) of the rectangular waveguide (meters)

- b: narrower dimension (narrow wall) of the rectangular waveguide (meters)
- m: mode index in the a-direction (integer, $m \geq 0$)
- n: mode index in the b-direction (integer, $n \geq 0$)

Equation 3.20 is also valid for f_c of higher-order modes in rectangular waveguides [28].

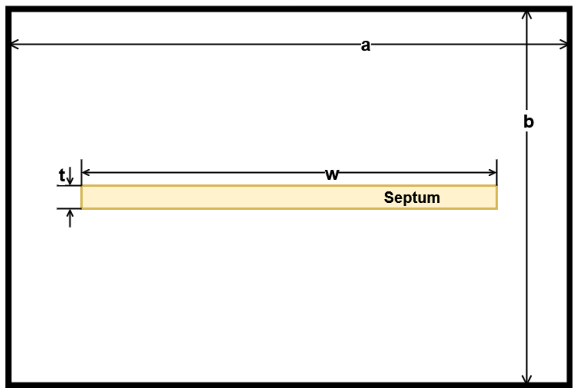

Figure 3.3 Geometrical arrangement of the TEM cell in the xy-plane.

The cutoff frequency of the TE_{10} mode equals $f_{c,10} = 3.75\,\text{GHz}$, according to Equation 3.20. A numerical approach yields the forward transmission coefficients between the output ports of the TEM cell S_{12} shown in Figure 3.4. There, the cut-off frequency f_c is defined as the smallest frequency point of undisturbed mode propagation (S_{12}= 0 dB).

Note for potential further work in this chapter: A paper by Wilson and Ma present analytical approximations to determine the cut-off frequencies [32]. There is a long list for the several first few corner frequencies of the first modes. Additionally, a paper by Koch, Groh and Garbe determines the resonance frequencies of the first TE modes analytically [14].

A TEM cell contains a tapered section at the output ports. TEM modes pass this section with a minimal amount of reflections. However, higher order TE and TM modes reflect from those sections, and because the TEM cell is a high-Q cavity, resonances occur at $\frac{\lambda}{4}$ and $\frac{\lambda}{2}$ [13].

Simulations with a tapered section have been done in [13]

plot title: $|S_{12}|$

Due to imperfections, change in materials or finite conductivity of the conducting plates, wave propagating in the TEM mode may excite higher order TE and TM modes [14]. A change in material, for example, demands the electric and magnetic field to have a component in the direction of propagation at the discontinuity, consequently exciting TM modes.

The TE_{10} and TE_{01} modes are non-essential modes with the lowest cut-off frequencies. Their transversal electric fields are depicted in Figure 3.5.

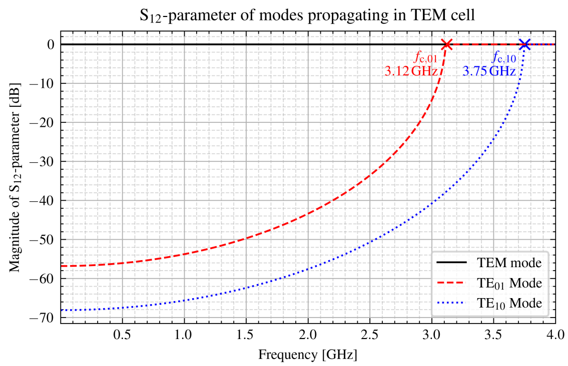

Figure 3.4 Propagation of TEM, TE_{01} and TE_{10} modes in the TEM cell. The black trace shows the S_{12}-parameter over the frequency of TEM mode. The blue trace demonstrates S_{12}-parameter of the TE_{10} mode. At a frequency of 3.75 GHz, this mode propagates without attenuation (S_{12}= 0), defining the cut-off frequency $f_{c,10}$. The simulated result comes very close to the analytically determined one. The red trace shows a cutoff frequency of $f_{c,10}$ = 3.12 GHz for the TE_{01} mode. Equation 3.20 would predict a cutoff frequency of 6.25 GHz, however, the septum influences n-odd modes like this one. Their cutoff frequencies are shifted to a lower value [28].

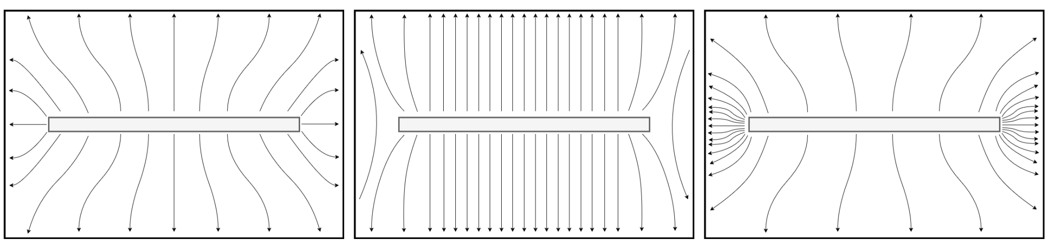

(a) TEM Mode **(b)** TE_{01} **(c)** TE_{10}

Figure 3.5 Transversal electric fields in cross section of TEM cell

Table 3.1 shows some cut-off frequencies of these modes for different TEM cell dimensions. A characteristic impedance of 50 Ω at the output ports is only kept in the case $a = 40$ mm and $b = 24$ mm.

a (mm)	b (mm)	TE_{01} f_c (GHz)	TE_{10} f_c (GHz)
80	24	1.89	2.05
40	24	3.17	3.76
40	48	2.10	3.76

Table 3.1 Cut-off frequencies of higher order modes at different TEM cell dimensions. The TE_{10}-mode is independent of the height b of the TEM cell, as would be the case in a rectangular waveguide. Both the TE_{10}-mode and the TE_{01}-mode are dependent on the width a.

3.3.4 Field distributions

The normalized electric field of the TEM mode is then given by Equation 3.21a in x-direction and by Equation 3.21b in z-direction [32]. The equations follow from the singular integral-equation approach in [29]. The formula is not valid for the gap regions. However, since there won't be any dipole moment placed there, this approximation will suffice. These equations are to understand the influence of electrically small structures, which do not align with the TEM modes, but still couple with the TEM cell and influence the results.

Is the series for several sine-waves fitting into the TEM cell, derived due to the nature of the Green's Function? If yes, then only the first-order must be used, since only the TEM mode is propagating. Now higher-order modes here.

$$e^{\pm}_{\mathrm{n,x}} = \frac{2}{a} Z_{\mathrm{w}}^{1/2} \sum_{m_0=1}^{\infty} \frac{\sinh M(b-py)}{\sinh Mb} \cdot \sin Mx \sin Ma \; J_0(Mg) \tag{3.21a}$$

$$e^{\pm}_{\mathrm{n,y}} = p\,\frac{2}{a}\, Z_{\mathrm{w}}^{1/2} \sum_{m_0=1}^{\infty} \frac{\cosh M(b-py)}{\sinh Mb} \cdot \cos Mx \; \sin Ma \, J_0(Mg) \tag{3.21b}$$

Formeln noch einmal überprüfen (TEM Zelle Geometrie beachten)

Hier würde ich gerne eine Tabelle mit Messwerten des normalisierten elektrischen Feldes in der TEM Zelle einfügen, wie es in [29] getan wurde

Z_{w} is the characteristic wave impedance, a the width of the TEM cell, b its height. The sign-function $p = 1$ above the septum, and $p = -1$ below it. $M = m\pi/2a$ and g is the distance between the gap between the septum and the conducting wall. The index $m = 1, 3, 5, ...$ is iterated over odd integers.

The normalized electric field intensity may be derived by the numerically resulting output power when placing dipole moments in the TEM cell. For example, Figure 3.7 demonstrates the output power of an electric dipole moment in the y-direction. It is shifted in the y-direction at center height between septum and upper TEM cell wall. Applying Equation 3.38a to the output power leads to the normalized magnitude of the field intensity in y-direction e_y.

The field distribution discussed are those of the TEM mode. In case of higher-order modes propagating, the field distribution is represented by a series of the mode fields.

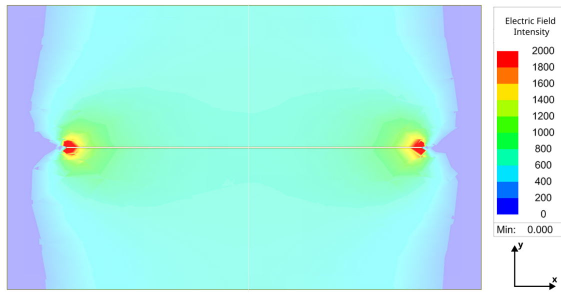

(a) Component of the normalized electric field distribution $\mathbf{e}^{\pm}_{\mathrm{TEM}}$ aligned in x-direction in TEM cell excited with 1/2 W at 3 GHz.

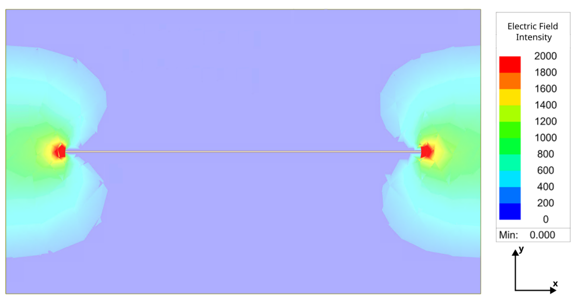

(b) Component of the normalized electric field distribution $\mathbf{e}^{\pm}_{\mathrm{TEM}}$ aligned in y-direction in TEM cell excited with 1/2 W at 3 GHz.

Figure 3.6

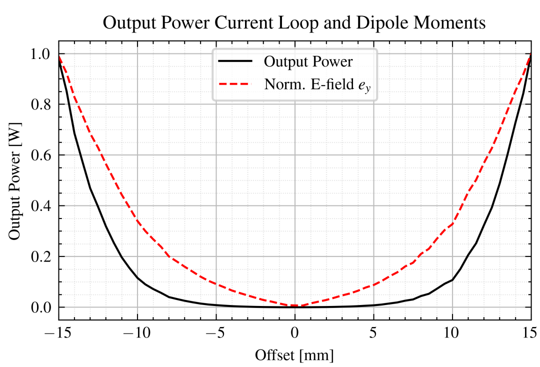

Figure 3.7 Output power and norm. E-field over offset. TODO: Move to numerical investigation chapter. Redo this simulation and correct plot labels. Plot Qualität erhöhen. Skalen anpassen.

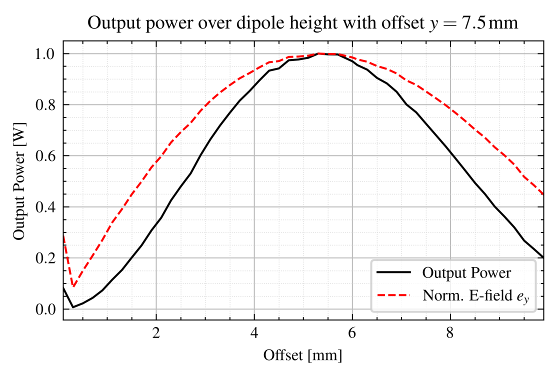

Figure 3.8 Output power and norm. E-field over height

Equation 3.22a shows that each mode is orthogonal to each other, with $\mathbf{e}_{\mathrm{n}}^{\pm}$ and $\mathbf{h}_{\mathrm{n}}^{\pm}$ being the function vectors of the electric and magnetic field in transverse direction [7]. This indicates that the modes do not couple with each other

A coupling between the modes only occurs due to geometric changes of the waveguide. $\mathbf{e}_n^{\pm}$ and $\mathbf{h}_n^{\pm}$ are normalized to $\sqrt{\mathrm{W}}$. Additionally, each mode is normalized to $\sqrt{\mathrm{W}}$, shown by Equation 3.22b. Only the transverse fields are investigated in these Equations, because they carry power along the waveguide, opposed to the fields in the propagation direction.

$$\iint \mathbf{e}_{\mathrm{n}}^{\pm} \times \mathbf{h}_{\mathrm{m}}^{\pm} \mathrm{d}\mathbf{s}' = 0 \quad \text{if} \quad n \neq m \tag{3.22a}$$

$$\iint \mathbf{e}_{\mathrm{n}}^{\pm} \times \mathbf{h}_{\mathrm{n}}^{\pm} \mathrm{d}\mathbf{s}' = 1 \tag{3.22b}$$

The radiated fields can be described by a summation of normal modes, as in **??** and **??**. The coefficients of these modes are straightforward to calculate, due to Lorentz Reciprocity Theorem, if the waveguide's walls are perfectly conducting. Ideally, any higher order mode than the first TEM mode will be suppressed, and the calculation simplifies to $n = 0$. Additionally, it is assumed that the source is electrically small, which makes it possible to represent it with dipoles, further simplifying the equations [15]. The fields radiated in the positive z-direction are

$$\mathbf{E}^{+} = \sum_n a_n \mathbf{e}_n^{+} \tag{3.23a}$$

$$\mathbf{H}^{+} = \sum_n a_n \mathbf{h}_n^{+}. \tag{3.23b}$$

And the fields propagating along the negative z-direction are [7, p. 360]

$$\mathbf{E}^{-} = \sum_n a_n \mathbf{e}_n^{-}, \tag{3.24a}$$

$$\mathbf{H}^{-} = \sum_n a_n \mathbf{h}_n^{-}. \tag{3.24b}$$

a_n and b_n are coefficents with unit $\sqrt{\mathrm{W}}$, which scale the normalized electric fields of each mode $\mathbf{e}_n^{\pm}$. The fields at the outputs $\mathbf{E}^{\pm}$ are decomposed therefore of several propagating modes, each weighted with the coefficients.

The normalized magnetic field intensity $\mathbf{h}_{\mathrm{n}}^{\pm}$ is derived similarly as $\mathbf{e}_{\mathrm{n}}^{\pm}$. In case of TEM mode

$$\mathbf{h}_{\mathrm{TEM}}^{\pm} = \frac{1}{Z_0} \hat{\mathbf{a}}_{\mathrm{z}} \times \mathbf{e}_{\mathrm{TEM}}^{\pm}, \tag{3.25}$$

where $Z_0 \approx 377\,\Omega$ is the free-space wave impedance.

3.4 Radiating Sources in TEM Cells

3.4.1 Arbitrary source

Suppose a current source $\mathbf{J}_1$ excites a waveguide (as is the case with the dipoles in the TEM cell). Normally, such a current source requires external fields to drive it, but for they are neglect for now. Only $\mathbf{E}$ and $\mathbf{H}$ are considered, which are the fields radiated by $\mathbf{J}_1$. $\mathbf{E}$ and $\mathbf{H}$ are solved according to $\nabla \times \mathbf{E} = -j\omega\mu_0\mathbf{H}$ and $\nabla \times \mathbf{H} = j\omega\epsilon_0\mathbf{E} + \mathbf{J}$ [7, p. 360]. Additionally, $\mathbf{e}_n^{\pm}$ and $\mathbf{h}_n^{\pm}$ are the resulting waveguide fields, with the signs indicating the direction of propagation. Take Equation 3.2 and set $\mathbf{J}_2 = \mathbf{M}_1 = \mathbf{M}_2 = 0$. Now, only the current source $\mathbf{J}_1$ remains, and the Equation 3.26 emerges.

$$\oiint_S (\mathbf{e}_n^{\pm} \times \mathbf{H} - \mathbf{E} \times \mathbf{h}_n^{\pm}) \cdot \mathrm{d}\mathbf{s}' = \iiint \mathbf{J_1} \cdot \mathbf{e}_n^{\pm} \mathrm{d}v' \tag{3.26}$$

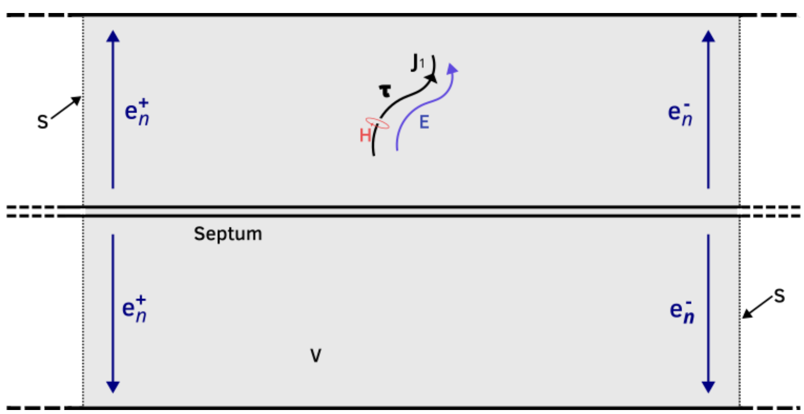

Figure 3.9 TEM cell with an arbitrary current source $\mathbf{J}_1$ along the curve $\boldsymbol{\tau}$. $\mathbf{E}$ and $\mathbf{H}$ are the field intensities induced by the current. $\mathbf{e}_n^+$ and $\mathbf{e}_n^-$ are outgoing fields towards both output ports of the TEM cell of arbitrary form. $\mathbf{S}$ indicates the surface, and V the volume of the domain in question.

TODO: Maybe add H fields in figure?

The fields $\mathbf{E}$ and $\mathbf{H}$ radiated by $\mathbf{J}_1$ equal a combination of normals modes. Using the expansions Equations (3.23a) and (3.23b), Equations (3.24a) and (3.24b) lead to

$$\begin{aligned}
&\oiint_S (\mathbf{e}_n^{+} \times \mathbf{H} - \mathbf{E} \times \mathbf{h}_n^{+}) \cdot \mathrm{d}\mathbf{s}' = \\
&\qquad = \oiint_S (\mathbf{e}_n^{+} \times \sum_m a_m \mathbf{h}_m^{+} - \sum_m a_m \mathbf{e}_m^{+} \times \mathbf{h}_n^{+}) \cdot \mathrm{d}\mathbf{s}' \\
&\qquad = \sum_m a_m \oiint_S (\mathbf{e}_n^{+} \times \mathbf{h}_m^{+} - \mathbf{e}_m^{+} \times \mathbf{h}_n^{+}) \cdot \mathrm{d}\mathbf{s}'.
\end{aligned} \tag{3.27}$$

Due to the orthogonal property of Equation 3.22a and the normalization in Equation 3.22b, the coefficients of each mode can be evaluated separately through

$$\oiint_S (\mathbf{e_n}^+ \times \mathbf{H} - \mathbf{E} \times \mathbf{h}_n^+) \cdot \mathrm{d}\mathbf{s}' =$$
$$= a_n \oiint_S (\mathbf{e}_n^+ \times \mathbf{h}_n^+ - \mathbf{e}_n^+ \times \mathbf{h}_n^+) \cdot \mathrm{d}\mathbf{s}' = -2a_n. \tag{3.28}$$

The coefficient b_n of the fields $\mathbf{e}_n^-$ and $\mathbf{h}_n^-$ are evaluated in the same manner.

In this equation, the wave amplitudes a_n and b_n are given through the surface integral in the Lorentz Reciprocity theorem, with a_n being the wave going to the left side, and b_n to the other.

One pair of coefficients a_{TEM}, b_{TEM} suffice when investigating the propagation of the TEM mode, only. The fields $\mathbf{e}_{\mathrm{TEM}}$ and $\mathbf{h}_{\mathrm{TEM}}$ of the TEM-mode are known . Combining them with Equation 3.22b leads to [31]

Some plot or table for explanation, plus citation

$$P_{\mathrm{out1}} = \iint_S \langle \mathbf{S} \rangle \cdot \mathrm{d}\mathbf{s}' = \iint_S \frac{1}{2} \Re\{(a \cdot \mathbf{e}_{\mathrm{TEM}}^{\pm}) \times (a \cdot \mathbf{h}_{\mathrm{TEM}}^{\pm})^*\} \cdot \mathrm{d}\mathbf{s}' = \frac{|a|^2}{2}, \tag{3.29a}$$
$$P_{\mathrm{out2}} = \iint_S \langle \mathbf{S} \rangle \cdot \mathrm{d}\mathbf{s}' = \iint_S \frac{1}{2} \Re\{(b \cdot \mathbf{e}_{\mathrm{TEM}}^{\pm}) \times (b \cdot \mathbf{h}_{\mathrm{TEM}}^{\pm})^*\} \cdot \mathrm{d}\mathbf{s}' = \frac{|b|^2}{2}. \tag{3.29b}$$

The Poynting vector $\langle \mathbf{S} \rangle$ of the TEM mode does not have an imaginary component,

$$\langle \mathbf{S} \rangle = \mathbf{e}_{\mathrm{TEM}}^{\pm} \times \mathbf{h}_{\mathrm{TEM}}^{\pm} = \Re\{\mathbf{e}_{\mathrm{TEM}}^{\pm} \times (\mathbf{h}_{\mathrm{TEM}}^{\pm})^*\}. \tag{3.30}$$

3.4.2 Equivalent dipole moments

The electric dipole moment $\mathbf{m_e}$ is given by the current $\mathbf{J}_1$ flowing through the infinitesimal wire.

$$\begin{pmatrix} a_n \\ b_n \end{pmatrix} = -\frac{1}{2} \mathbf{m_e} \cdot \mathbf{e}_n^{\pm} \tag{3.31}$$

If this arbitrary current distribution forms an infinitesimal loop, the source can be represented by a magnetic dipole moment $\mathbf{m_m}$. It is defined by the product $\mathbf{m_m} = \mathbf{A} \cdot I$, an infinitesimal current loop with area A carrying a current I. This leads to Equation 3.32. This formulation assumes, that the magnetic field strength $\mathbf{h}^{\pm}$ does not change over the loop area, i.e. the loop is electrically small. Otherwise, the magnetic field strength $\mathbf{h}^{\pm}$ must be considered in the integration [7, 24].

$$\begin{aligned}\begin{pmatrix}a_n\\b_n\end{pmatrix} &= -\oint_C \mathbf{e}_n^{\pm}\mathrm{d}l\\ &= -\iint_S \nabla\times\mathbf{e}_n^{\pm}\mathrm{d}\mathbf{s}'\\ &= \mathrm{i}\omega\mu_0\iint_S \mathbf{h}_n^{\pm}\cdot\mathrm{d}\mathbf{s}'\\ &= \mathrm{i}\omega\mu_0\mathbf{m}_m\mathbf{h}_n^{\pm}\end{aligned} \tag{3.32}$$

If there are several modes propagating, it is useful to find the coefficients of the modes a_n and b_n in **??** and **??**. In this case, the orthogonality property in Equation 3.22a is used to derive Equation 3.33a and Equation 3.33b [7]. The wire is described by a curve C, and the tangential vector $\boldsymbol{\tau}$ is used to integrate along this curve.

$$2a_n = -\int_C \boldsymbol{\tau}\cdot\mathbf{e}_n^{-}\mathrm{d}l \tag{3.33a}$$

$$2b_n = \int_C \boldsymbol{\tau}\cdot\mathbf{e}_n^{+}\mathrm{d}l \tag{3.33b}$$

An electrically small radiating source may be represented by six dipoles. This number includes three magnetic dipoles pointing in every direction of the Cartesian coordinate system (x, y, and z-direction), and three electric dipoles in the same orientation. Consequently, an equipment under test (EUT) could be modeled with these dipoles, leading to much less computational effort in simulation. The excited EM waves by point sources is discussed in [7] and in subsection 3.3. An analytical procedure to determine these dipole moments is presented by Sreenivasiah [24], and some experimental results based on it can be found in the research of Kreindl, where bond wires were modeled with magnetic dipoles[17], and, again, Sreenivasiah [24].

The idea is to place the EUT in the TEM cell and measure the power of both output ports. The amplitudes of the TEM fields are expressed by Equation 3.34 [24].

$$\begin{pmatrix}a_n\\b_n\end{pmatrix} = \frac{1}{2}(-\mathbf{m_e}\cdot\mathbf{e}_n^{\pm} + \mathrm{i}\omega\mu_0\mathbf{m_m}\cdot\mathbf{h}_n^{\pm}) \tag{3.34}$$

The magnetic field $\mathbf{h}_n$ and electric field $\mathbf{e}_n$ are both normalized to $1\sqrt{\mathrm{Hz}}$ [17] and correspond to the TEM mode in free space [24]. The electric dipole moment $\mathbf{m_e}$ and the magnetic dipole moment $\mathbf{m_m}$ are complex vectors, containing an amplitude and phase for every one of the three directions in the coordinate system (x, y, z), and have the units $\mathrm{A}\cdot\mathrm{m}$ and $\mathrm{V}\cdot\mathrm{m}$. The variables a and b correspond to the amplitudes of the waves in both possible directions in the TEM cell with the unit $\sqrt{\mathrm{W}}$. This leads to the final form in Equation 3.35 [24].

$$\begin{pmatrix}a_n\\b_n\end{pmatrix} = -\frac{1}{2}(\mathbf{m_e}\pm jk\mathbf{m_m}\times\mathbf{z})\cdot\mathbf{e}_n^{\pm}. \tag{3.35}$$

$\mathbf{m}_\mathrm{e}$ and $\mathbf{m}_\mathrm{e}$ are separately derived by

$$\mathbf{m}_\mathrm{e} = \frac{a_n + b_n}{\mathbf{e}_n^{\pm}}, \tag{3.36}$$

$$\mathbf{m}_\mathrm{m} = j\frac{a_n - b_n}{k_0 \mathbf{e}_n^{\pm}}. \tag{3.37}$$

The unity vector $\hat{\mathbf{a}}_z$ points in direction of propagation. The function vector $\mathbf{e}_n^{\pm}$ describes the normalized electric field amplitude in traverse direction, i.e. x and y-directions, of the excited fundamental mode. Due to the normalization of the electric and magnetic fields to $1\sqrt{\mathrm{W}}$, the total power at one port is $1/2\,\mathrm{W}$. This defines $\mathbf{e}_n^{\pm}$ as the electric field of the TEM cell, excited with a peak unit power (1 W).

The individual components aligned with the x- and y-direction can be investigated separately. For example, the components of $\mathbf{m}_\mathrm{e}$ are derived with

$$m_\mathrm{ex} = \frac{2\sqrt{P_\mathrm{x}}}{e_\mathrm{n,x}^{\pm}}, \tag{3.38a}$$

$$m_\mathrm{ey} = \frac{2\sqrt{P_\mathrm{y}}}{e_\mathrm{n,y}^{\pm}}. \tag{3.38b}$$

P_x and P_y describe the power measured at one output port induced by the respective component of the dipole moment [24]. The output power generated by a component of the dipole moment depends on $\mathbf{e}_\mathrm{n}^{\pm}$, therefore on the position in the TEM cell.

The electric dipole in the TEM cell leads to a increase in power with the same phase in both ports, and a magnetic dipole leads to the same increase, but with a phase shift of 180°. This is due to the phase-shift of the magnetic fields at the output ports, as shown in Figure 3.10. The EUT shall be place halfway on the septum in z-direction to accurately derive electric and magnetic dipole moments.

It is required to measure the power at the output ports with phase information, which is done with the complex Poynting vector in a numerical analysis. When measuring an EUT with a real TEM cell, the phase information may be found by summing and subtracting the output powers of the ports, as is shown in [24].

3.4.3 Electrically small antennas

The electric field coupling with an electrically small antenna can be simply put as [7, p. 361]

$$2a_n = -\int_C \boldsymbol{\tau} I(l) \cdot \mathbf{e}_n^{+}\, dl. \tag{3.39a}$$

$$2b_n = -\int_C \boldsymbol{\tau} I(l) \cdot \mathbf{e}_n^{-}\, dl. \tag{3.39b}$$

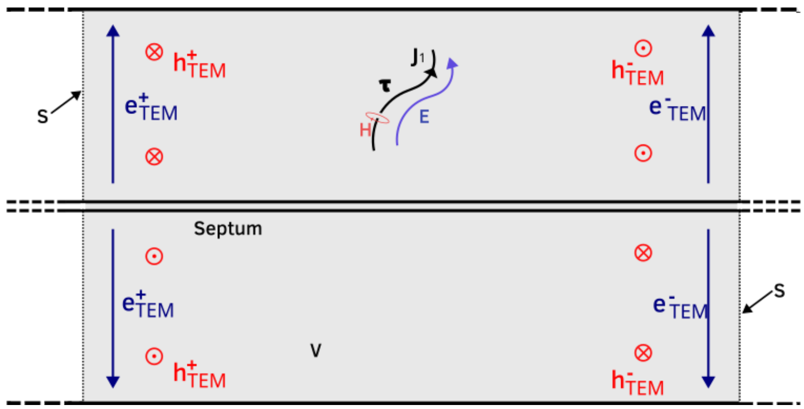

Figure 3.10 Field distribution of the TEM mode highlighting the out-of-phase magnetic fields at the output ports.

Since the antenna is electrically small, the electric field $\mathbf{e}_n^{\pm}$ is assumed to be constant in C. Furthermore, if the current I is constant along C, it does not have to be considered in the integration. Integrating over the closed loop simplifies to [7, p. 361]

$$2a_n = -\oint_C \mathbf{e}_n^+ \cdot \boldsymbol{\tau}\, dl = j\omega\mu_0 \iint_S \mathbf{h}_n^+\, d\mathbf{s}' = V_n^+, \tag{3.40a}$$

$$2b_n = -\oint_C \mathbf{e}_n^- \cdot \boldsymbol{\tau}\, dl = j\omega\mu_0 \iint_S \mathbf{h}_n^-\, d\mathbf{s}' = V_n^-. \tag{3.40b}$$

The induced voltage V_n^+ causes or is caused by the fields at one port $\mathbf{e}_n^+$, $\mathbf{h}_n^+$, and the induced voltage V_n^- by the fields at the other port $\mathbf{e}_n^-$, $\mathbf{h}_n^-$. The induced voltages V_n^+ and V_n^- relate to the magnetic dipole moment $\mathbf{m_m}$ and the coefficients a and b. Defining a total induced voltage as $V_n = V_n^- - V_n^+$ leads to

$$\mathbf{m}_m = \frac{a_n - b_n}{\mathbf{e}_n^{\pm} \cdot k_0} = \frac{V_n}{\mathbf{e}_n^{\pm} \cdot k_0}. \tag{3.41}$$

A magnetic dipole moment $\mathbf{m}_m$ producing fields characterized with coefficients a_n and b_n models the magnetic coupling behavior of any electrically small antenna yielding the same coefficients. Consequently, deriving an equivalent $\mathbf{m}_m$ of an electrically small antenna is possible by measuring $a_n - b_n$ at the output port.

In a similar manner to Equations (3.39a) and (3.39b), a constant magnetic field $\mathbf{h}_n^{\pm}$ along C, where a magnetic current is present, leads to

$$2a_n = -\int_C \boldsymbol{\tau} I_m(l) \cdot \mathbf{h}_n^+\, dl, \tag{3.42a}$$

$$2b_n = -\int_C \boldsymbol{\tau} I_m(l) \cdot \mathbf{h}_n^-\, dl. \tag{3.42b}$$

Analogous to Equations (3.40a) and (3.40b), I_m is assumed to be constant and C to form a closed loop, leading to

$$2a_n = -\oint_C \mathbf{h}_n^- \cdot \boldsymbol{\tau}\, dl = -j\omega\epsilon_0 \iint_{S_0} \mathbf{e}_n^+ \, d\mathbf{s}', \tag{3.43a}$$

$$2b_n = -\oint_C \mathbf{h}_n^+ \cdot \boldsymbol{\tau}\, dl = -j\omega\epsilon_0 \iint_{S_0} \mathbf{e}_n^- \, d\mathbf{s}'. \tag{3.43b}$$

Now, further surfaces S_1 and S_2 are defined. Surface S_1 leads, starting from S_0, parallel to the electric field $\mathbf{e}_n^\pm$ to infinity. A total surface is defined $S = S_0 + S_1 + S_2$, where S_2 closes the total surface around S_1 in infinity. Therefore, the total surface covered is closed, and Equations (3.43a) and (3.43b) can be written as

sketch

$$j\omega\epsilon_0 \oiint_S \mathbf{e}_n^\pm \cdot d\mathbf{S} = j\omega\epsilon_0 \iint_{S_0} \mathbf{e}_n^\pm \cdot d\mathbf{S} + \underbrace{j\omega\epsilon_0 \iint_{S_1} \mathbf{e}_n^\pm \cdot d\mathbf{S}}_{=0} + \underbrace{j\omega\epsilon_0 \iint_{S_2} \mathbf{e}_n^\pm \cdot d\mathbf{S}}_{=0}. \tag{3.44}$$

Inserting Gauss' law $\nabla \cdot \mathbf{E} = \frac{\rho}{\epsilon_0}$ leads to

$$-j\omega\epsilon_0 \oiint_S \mathbf{e}_n^\pm \cdot d\mathbf{s}' = -j\omega\epsilon_0 \iiint_V \nabla \cdot \mathbf{e}_n^\pm \cdot dv' = -j\omega \iiint_V \rho_n^\pm \cdot dv'. \tag{3.45}$$

With the continuity equation $j\omega\rho = -\nabla \cdot \mathbf{J}$ this leads to

$$2a_n = -j\omega \iiint_V \rho_n^+ \cdot dv' = \iiint_V \nabla \cdot \mathbf{J}_n^+ \cdot dv' = \oiint_S \mathbf{J}_n^+ \cdot d\mathbf{s}' = I_n^+, \tag{3.46a}$$

$$2b_n = -j\omega \iiint_V \rho_n^- \cdot dv' = \iiint_V \nabla \cdot \mathbf{J}_n^- \cdot dv' = \oiint_S \mathbf{J}_n^- \cdot d\mathbf{s}' = I_n^-. \tag{3.46b}$$

Relating the obtained expression to the electric dipole moment from Equation 3.36 with a total current $I_n = I_n^+ + I_n^-$ delivers

$$\mathbf{m}_e = \frac{a_n + b_n}{\mathbf{e}_n^\pm} = \frac{I_n}{\mathbf{e}_n^\pm}. \tag{3.47}$$

The physical meaning of I_n is electrical current passing between the septum and the dipole through capacitive coupling with a certain mode, i.e. displacement current. Concluding, the magnetic dipole moment occurs due to induced voltage, while the electric dipole moment due to coupling electric current.

An electric dipole moment $\mathbf{m}_e$ producing fields characterized with coefficients a_n and b_n models the electric coupling behavior of any electrically small antenna yielding the same coefficients. Consequently, deriving an equivalent $\mathbf{m}_e$ of an electrically small antenna is possible by measuring $a_n + b_n$ at the output port.

Numerical simulations enable the determination of $a+b$ and $a-b$ directly. When applying this described method in a measurement with a real TEM cell, the values are found by adding and subtracting the output powers of both ports, as is shown in [24].

3.4.4 Radiation resistance

TODO: Wird dieses Unterkapitel gebraucht?

The radiation resistance of an electrically small antenna is derived by applying the Green's function. The following content is mostly taken from [30].

To analyze the fields in a TEM cell, the dyadic Green's function discussed in subsubsection 3.2.2 proofs itself to be useful. It is assumed, that a vertical, electrically short antenna is inserted in the top center of the TEM cell. This is modeled by a current distribution in y-direction $\hat{\mathbf{J}}(\mathbf{x}) = \mathbf{a}_y J(\mathbf{x})$ [30]. Accordingly, the Green's function reduces to $\hat{\mathbf{G}}(\mathbf{x}, \mathbf{x}') = \mathbf{a}_y G(\mathbf{x}, \mathbf{x}')$. First, the Green's function for a rectangular waveguide $G_O(\mathbf{x}, \mathbf{x}')$ is shown in Equation 3.48 [2]. There, η_0 is the free-space impedance, $M = m\pi/(2a)$, $N = n\pi/b$ and $K_m = (\xi^2 - M^2)^{1/2}$. Furthermore,

Check Vector notation. Is correct for Dyadics?

$$\Delta_n = \begin{cases} \frac{1}{2}, & n = 0 \\ 1, & n > 0 \end{cases}$$

and,

$$g_{mn}(\mathbf{x}_t, \mathbf{x}_t') = \left(\tfrac{2}{ab}\right) \sin M(x+a) \sin M(x'+a) \cdot \cos Ny \cos Ny'$$

are functions implemented in Equation 3.48. The components x, x' and y, y' are part of the vectors $\mathbf{x}_t$, $\mathbf{x}_t'$.

$$\tilde{G}_0(\mathbf{x}_t, \mathbf{x}_t') = \frac{-\mathrm{j}\eta_0}{k_0} \left\{ \sum_{m,n=0}^{\infty} \frac{\Delta_n [M^2 + \beta^2]}{M^2 + N^2 - \xi^2}\, g_{mn}(\mathbf{x}_t, \mathbf{x}_t') \right\} \tag{3.48}$$

The TEM cells Green's function by adding a unperturbed term to it [30]. The derivation of those Green's Functions is demonstrated in [29], which uses the same methods described in [2], as mentioned above.

The perturbed term in Equation 3.49 describes the influence of the gaps on the field distribution. They are derived by forcing the tangential fields to be continuous across the gaps, then describing this boundary condition mathematically as a perturbing second Green's function. The rest of the boundary conditions on the are zero due to the geometry of the TEM cell. The functions used are,

$$L(\beta) = \left[\ln\left(\frac{8a}{\pi g}\right) - \frac{\pi}{a} \sum_{m \in \{1,3,5,\ldots\}}^{\infty} \left(\frac{\cot K_m b}{K_m} + \frac{2a}{m\pi} \right) \right]^{-1}$$

and,

$$f(\mathbf{x}_t) = \sum_{m \in \{1,3,5,\dots\}}^{\infty} M \frac{\cos K_m(b-y)}{K_m \sin K_m b} \sin Ma \cos Mx J_0(Mg).$$

To receive the final Green's Function, the unperturbed and perturbed term are added together $G(\mathbf{x}_t, \mathbf{x}'_t) = G_O(\mathbf{x}_t, \mathbf{x}'_t) + G_g(\mathbf{x}_t, \mathbf{x}'_t)$. Naturally, the observation point $\mathbf{x}$ can only be on the upper half in the chamber, where the source is also located [30].

$$\widetilde{G}_g(\mathbf{x}_t, \mathbf{x}'_t) = \frac{-j\pi k_0 \eta_0}{2a^2 s^2} L(\beta) f(\mathbf{x}_t) f(\mathbf{x}'_t) \tag{3.49}$$

Because waves propagating in the TEM cell are assumed to travel into infinity, they might have any longitudinal propagation constant β. They are not limited by boundary conditions in this direction. It therefore proofs useful to apply a Fourier Series over this variable, as done in Equation 3.50. There, the subscript t indicates only the transverse (xy-plane).

This explanation is not directly cited but my interpretation. Make sure that this is correct info.

$$G_O(\mathbf{x}, \mathbf{x}') = \frac{1}{2\pi} \int_{-\infty}^{\infty} \tilde{G}_0(\mathbf{x_t}, \mathbf{x'_t}) \mathrm{e}^{j\beta z} \mathrm{d}\beta \tag{3.50a}$$

$$G_g(\mathbf{x}, \mathbf{x}') = \frac{1}{2\pi} \int_{-\infty}^{\infty} \tilde{G}_g(\mathbf{x_t}, \mathbf{x'_t}) \mathrm{e}^{j\beta z} \mathrm{d}\beta \tag{3.50b}$$

Now, the antenna impedance is calculated using the generic Equation 3.51. The Green's Function in this represents the electric field excited by an unit strength dipole [30]. Scaled by multiplication with the current density $\mathbf{J}(\mathbf{x})$ and integrated over the length of the wire, results in the total electric field. Next, by multiplying it by the current distribution $\mathbf{J}(\mathbf{x})$ and integrated over the length of the wire again, leads to the apparent power. In the end, dividing this term by the total current consumption squared I^2 leads to the impedance.

$$Z = \frac{-1}{I^2} \int_S \int_{S'} \mathbf{J}(\mathbf{x}) \cdot \mathbf{G}(\mathbf{x}, \mathbf{x}') \cdot \mathbf{J}(\mathbf{x}') \, \mathrm{d}s' \, \mathrm{d}s \tag{3.51}$$

When evaluating the real part of the impedance for the case described here, the radiation resistance results from Equation 3.52. If the inserted antenna is electrically small, as it is in this case, d reduces the influence of other terms. The most dominant term then, k_0^2, results in a quadratic relation of the radiation resistance to the frequency. This agrees with the theoretical framework in the discussion about small dipoles in **??**, as well as with the simulations results in section 4.

$$R = \frac{\pi \eta_0 k_0^2}{4a^2} \csc^2 k_0 d \, L(k_0) H(k_0) \tag{3.52}$$

Here,

$$H(\beta) = \sum_{m' \in \{1,3,5,\dots\}}^{\infty} h_{m'}(\beta) \sum_{m \in \{1,3,5,\dots\}}^{\infty} h_m(\beta) J_0(r(M^2 + \beta^2)^{1/2})$$

and,

$$h_m(\beta) = \frac{M \sin MaJ_0(Mg)}{K_m \sin K_m b} \cdot \frac{\cos k_0 d - \cos K_m d}{M^2 + \beta^2}.$$

3.5 Shielding

Effective shielding is of great interest to reduce EMI of electronic systems. A figure of merit for shielding capabilities of a material is the electromagnetic shielding effectiveness (SE), given in Equation 3.53 [8]. E_i is the incident electric field, while E_t is the transmitted electric field, also depicted in Figure 3.11. It depends on the thickness and shape of the material, and its electric and magnetic properties. Additionally, the TEM cell contributes to the SE values.

$$SE_\mathrm{dB} = 20 \log \left(\frac{E_\mathrm{i}}{E_\mathrm{t}}\right) \tag{3.53}$$

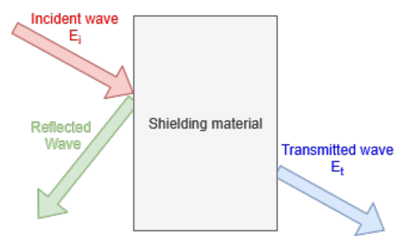

Figure 3.11 Incident, reflected and transmitted electric fields due to interaction with shielding material

An electromagnetic wave may undergo several reflections inside the shielding material, with each reflection adding up to the total reflected, absorbed and transmitted waves. The total shielding effectiveness is therefore determined by Equation 3.54, according to Schelkunoff. A_dB represents the absorption losses traveling through the shield, R_dB the reflection losses, and B_dB is the correction factor for the multiple reflections inside the shield [8].

$$SE_\mathrm{dB} = R_\mathrm{dB} + A_\mathrm{dB} + B_\mathrm{dB} \tag{3.54}$$

Calculate with S-params S_{11} and S_{21}: A, R and T.

This approach to shielding with internal re-reflections in the shielding material was derived by Schelkunoff. `https://www.ieee.li/pdf/viewgraphs/fundamentals_electromagnetic_shield.pdf`

The reflections occur due to the change in wave impedance. They are described through a reflection coefficient R. Additionally, it is common to normalize the wave impedance Z to the free-space wave impedance Z_0. At the interface from free-space to a shielding material, this leads to Equation 3.55 [7].

$$R = \frac{Z-1}{Z+1} \tag{3.55}$$

$$Z = \frac{1}{Z_0}\sqrt{\frac{\mathrm{i}\omega\mu}{\sigma + \mathrm{i}\omega\epsilon}} \tag{3.56}$$

The reflection coefficient can be converted into dB, leading to R_{dB}. Any additional reflection happen due to re-reflections inside the shielding material, described by B_{dB}. The rest of the energy must either be absorbed, described by A_{dB} or transmitted, shown by T_{dB}.

The wave number k in lossy media is described in a real an imaginary parts as in Equation 3.57. The imaginary part α is the attenuation or absorption coefficient. It describes the reduction of the intensity of the wave, which occurs with $\mathrm{e}^{-\alpha x}$, where x is the coordinate direction of propagation. The real part $\beta = \frac{2\pi}{\lambda}$ is the phase constant [12].

$$k = \beta + \mathrm{i}\frac{\alpha}{2} \tag{3.57}$$

$$\mathbf{E} = \mathbf{e} \cdot \mathrm{e}^{-jkx} \tag{3.58}$$

When the molecules in a material are exposed to electric fields, they will polarize, described by their permittivity ϵ. When exposed to a magnetic field, the spinning of their electrons in the atoms align with the magnetic field, described by the permeability μ of the material. When the fields alternate over time, the molecules will always move and align according to them. This is essentially a movement of charges, and therefore described by a conductivity σ. The energy lost in this process is dissipated as heat [1].

The electric field will push charges in polarizable molecules apart. This separation of charges may be described as a electric dipole, depending on the separation distance and the charge. Under alternating electric fields, the moving of charges will contribute to σ. This phenomenon is called dielectric hysteresis. Equation 3.59 quantifies it by a loss tangent $\tan\delta_e$ [1]. There, σ_s is the static conductivity, meaning the conductivity of the material for static fields. The complex part of the permittivity ϵ'' describes the lossy part of the dielectric material, specifically relevant for the alternating fields case. The real part of the permittivity is lossless and is noted by ϵ'. The overall complex permittivity is therefore $\epsilon = \epsilon' + \mathrm{i}\epsilon''$.

$$\tan\delta_e = \frac{\sigma_s}{\omega\epsilon'} + \frac{\epsilon''}{\epsilon'} \tag{3.59}$$

The loss tangent therefore $\tan\delta_e$ relates the conductivity of a material to the real permittivity. A dielectric with low losses has a much larger displacement current than conduction current density ($\tan\delta_e \ll 1$). The opposite is true for a good conductor ($\tan\delta_e \gg 1$) [1].

The loss tangent $\tan\delta_e$ is a function of frequency, however, it is often not stated as such. Therefore, the loss tangent of FR4, for example, is given as $\tan\delta_e = 0.02$ for frequencies up to 1 GHz. For higher frequencies, the molecules may have resonance frequencies,

p. 309 Classical Electrodynamics (John David Jackson) describe shielding material by dipole moments

Formula α? Needed?

S-parameters should enable derivation of α. Due to normal incident wave of TEM, no angle needed to consider.

Basics: Balanis 2012 page 68?

Some way to describe coupling of shielding material to TEM cell?

where they influence more strongly the overall conductance and consequently increase the imaginary part of the permittivity ϵ''.

There are also magnetically lossy materials, which is introduced by a complex permeability $\mu = \mu' + \mathrm{i}\mu''$. Analog to the dielectric case, the permeability can also be described by a loss tangent $\tan\delta_m$ as shown in Equation 3.60. However, the loss tangent is very low for the majority of materials and will be neglected. Ferrites are an exception, which are commonly used to dampen high frequency signals [1].

$$\tan\delta_m = \frac{\mu''}{\mu'} \tag{3.60}$$

Electric fields dominate in the near-field region of electric dipoles. To shield them, high permittivity and high conductivity materials, ideally with a high loss tangent $\tan\delta_e$ shall be used. On the other hand, magnetic fields dominate in the near-field region of magnetic dipoles. For shielding them, high permittivity and high conductivity materials, again with a high loss tangent $\tan\delta_m$ shall be used.

describe α and δ for absorption. Then reflections with ϵ and μ

source

3.5.1 ASTM ES7-83 Method

The ASTM ES7-83 method is used to determine the shielding effectiveness of shielding materials. The shielding material is inserted into a coaxial TEM cell around the septum. Ideally, they form a continuous connection [22].

In this method, two measurements are performed with an oscilloscope attached to the output of the TEM cell. In the first, an empty TEM cell is excited and a reference output voltage U_{ref} is measured. In the second, the TEM cell is loaded with the shielding material, and the output voltage U_{load} is again noted. The measurement values are then used in Equation 3.61 to derive the shielding effectiveness SE_{dB} [22].

$$SE_{\text{dB}} = 20 \cdot \log\left(\frac{U_{\text{ref}}}{U_{\text{load}}}\right) \tag{3.61}$$

In the case of simulating the problem, such a procedure may be used, too. It is more convenient, then, to defined a reference output power P_{ref} for an unloaded TEM cell, and a output power for the loaded case P_{load}. This leads to the similar Equation 3.62.

$$SE_{\text{dB}} = 10 \cdot \log\left(\frac{P_{\text{ref}}}{P_{\text{load}}}\right) \tag{3.62}$$

Additionally, a rectangular TEM cell is used for this method, instead of the commonly used cylindrical version. Figure 3.12b shows the cross section of this shielding material, which is inserted into the TEM cell. In Figure 3.12a the shielding material can be seen wrapped around the septum.

Then, the S-parameters derived in the simulations are used to get to the output powers P_{ref} and P_{load}. By exciting the TEM cell with a power of 1 W, the reference power $P_{\text{ref}} = 1\,\text{W}$. The measured power is then derived through Equation 3.63.

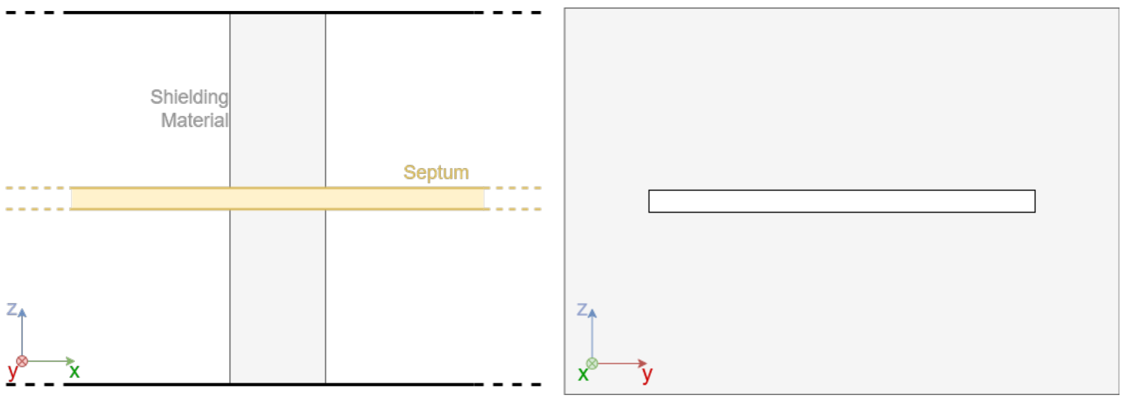

(a) Shielding material in TEM cell **(b)** Shape of the shielding material

$$P_{\text{load}} = P_{\text{ref}} \cdot 10^{|S_{12}|/10} \tag{3.63}$$

Describe Method. Then follows dual TEM cells

3.5.2 Dual TEM cell

The shielding effectiveness of a material may also be determined using two TEM cells, which are stacked upon each other, as shown in Figure 3.13. They are connected through an aperture, which can be filled with the shielding material. One TEM cell is excited, and therefore acts as a driving cell. It transmits power through the aperture. It is measured at the second TEM cell, which acts as a receiver. The dual TEM cell simulates near-field conditions, opposed to the far-field conditions simulated by the simple TEM cell [22].

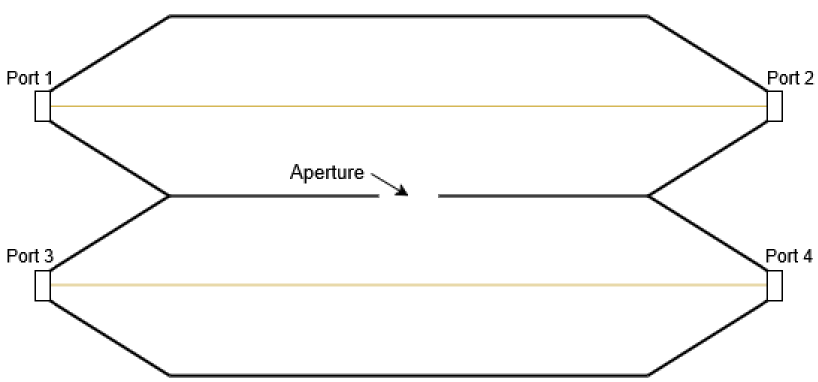

Figure 3.13 Dual TEM cell with aperture

The electrically small aperture may be described by an electric and a magnetic dipole moment. Their magnitude is related to the electric and magnetic coupling between the TEM cells over the aperture. Therefore, the electric and magnetic coupling can be determined separately by adding or subtracting the output powers of the receiving TEM cell [22, 31]. Consequently, a electric shielding effectiveness $SE^{\mathrm{e}}_{\mathrm{dB}}$ can be calculated with Equation 3.64a, and a magnetic shielding effectiveness $SE^{\mathrm{m}}_{\mathrm{dB}}$ with Equation 3.64b. If a material, for example, permits energy transfer because of magnetic dipoles in it, then a measurement with lower $SE^{\mathrm{m}}_{\mathrm{dB}}$ than $SE^{\mathrm{e}}_{\mathrm{dB}}$ is to be expected [31].

why must it be electrically small?

$$SE^{\mathrm{e}}_{\mathrm{dB}} = 10\log\left(\frac{P_{\mathrm{ref,sum}}}{P_{\mathrm{load,sum}}}\right) \tag{3.64a}$$

$$SE^{\mathrm{m}}_{\mathrm{dB}} = 10\log\left(\frac{P_{\mathrm{ref,diff}}}{P_{\mathrm{load,diff}}}\right) \tag{3.64b}$$

Because the normalized electric field at the aperture will be of TEM mode, only the component normal to the aperture in z-direction has to be considered. Just as in the case of dipole representation, the Lorentz Reciprocity theorem may be applied to find the fields in the TEM cell. Because both the fields at the output and in the aperture are of TEM mode, only the E-field at the output may be considered.

Since the aperture is electrically small, the field quantities may be assumed to be constant over it. This makes it possible to represent the energy transfer by dipole moments.

Polarization of the material. Small aperture theory.

4 Finite Element Method

4.1 General Idea

Problems involving the calculations of electromagnetic fields are often cumbersome and difficult to solve. This is due to the need of solving differential equations describing these fields over a computational domain, which is not possible with a computer in this sense. The simulation software Ansys HFSS (High Frequency Simulation Software) aims to provide a solution. This software is used for the simulations in section 4, hence it is described in this following, dedicated section.

HFSS uses a numerical technique, namely the Finite Element Method (FEM). The general idea of FEM after Rayleigh-Ritz-Galerkin is to choose a number of basis functions. The goal is to find a linear combination of these basis functions, so that the differential equation is satisfied as closely as possible. This turns the problem of solving a differential equation into a system of algebraic equations, which the computer can process. There is always a set of basis functions which enable the calculation to converge to the real solution. However, the number of basis functions used in the domain is limited, due to reasons of computability [25].

FEM therefore divides the domain into finite elements, i.e. smaller pieces. Then, within each piece, such a basis function is assigned. A linear combination of these basis functions are found, which satisfy the differential equations. In region where the approximating solution has a high degree of error, the accuracy may be increased by further subdividing the finite elements. This is repeated, until the error falls below a certain threshold, and a precise solution is derived.

4.2 Dividing a computational domain into finite elements

The differential equation to be solved is shown in Equation 4.1, where ϵ_r is the relative permeability and μ_r is the relative permeability of the material. The variable k_0 is the wave number of free space and equals $k_0 = \omega\sqrt{\epsilon_0\mu_0}$. [6, 19, 5].

$$\nabla \times \left(\frac{1}{\mu_r} \nabla \times \mathbf{E} \right) - k_0^2 \epsilon_r \mathbf{E} = 0 \quad \text{in } \Omega \tag{4.1}$$

This equation is solved in a computational domain Ω. This computational domain is divided into finite elements, called a mesh. Each node in this mesh has polynomial functions assigned, which are weighted to approximate the real solution. It has been proven that tetrahedral finite elements are best suited for this task, as they are geometrically flexible and make the definition of complete polynomial approximation functions possible [23]. Ansys HFSS uses a adaptive finite element mesh generator, which automatically provides a mesh for a given 3-dimensional construction. The Delaunay tesselation for three-dimensions is used for generating a mesh. It efficiently creates a mesh from objects of arbitrary shapes. Any boundary condition can be added recursively to the mesh. At the heart of this algorithm lies the property, that the circumsphere of an tetrahedra's vertices may not contain other tetrahedra's vertices.

Figure 4.1 shows one of such tetrahedrons. At the edge points, the components of the field which are normal to the respective edge and tangential to the face of the element is stored. At the vertex points, the component of a field which are tangential to the edges are stored. The value of the field at any midpoint is derived through interpolation from the node values. The basis function is used for interpolation.

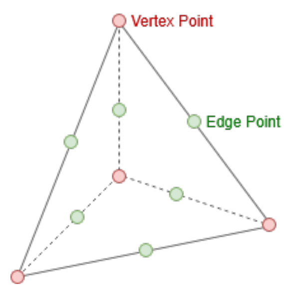

Figure 4.1 Tetrahedron with points on the edge and vertices.

Because of the way how the fields are stored in the tetrahedra, they are called tangetial vector finite elements. Their advantage is that tangential components of fields can be forced to be equal among adjacent tetrahedra at the boundary. For example, an electric field stored at a vertex point must point in the direction along one of the edges, therefore it is tangential to the element. An adjacent element then has the same tangential electric field imposed at this node, leading to a continuous tangential electric field, therefore satisfying the boundary conditions implied by the Maxwell equation automatically. Furthermore, any Dirichlet boundary conditions can easily be set along the edges. [19].

The finite element is described as Equation 4.2, where $L_2(\Omega)$ is a set of square integrable functions and P_1 a set of piecewise linear functions in the discretized domain Ω [20]. The vector fields at the vertices are given as u. $D(\Omega)$ is a set of divergence free functions. The vectors u used in the finite element therefore

- are continuous in the normal direction.

- are square integrable.
- have a curl describable by piecewise linear functions.

$$H_1^{(\text{dim}=3)}(\text{curl}) = \left\{ \mathbf{u} \mid \mathbf{u} \in [L_2(\Omega)]^3, \nabla \times \mathbf{u} \in [P_1(\Omega)]^3 \cap D(\Omega) \right\} \tag{4.2}$$

Figure 4.2 shows the finite element with the unknowns marked at each point. For reasons of simplicity, only the face is shown. The variables u_i^j and u_j^i are imposed across element boundaries, therefore guaranteeing tangential continuity at boundaries. Additionally, they inherently defined a linear polynomial, meaning that they describe a gradient of the field along this edge. Equation 4.3 describes this relation mathematically, where $\mathbf{t}_{ij}$ is the unit vector tangentially to the edge from node i to node j and l_{ij} is the length of this edge.

$$\mathbf{u} \cdot \mathbf{t}_{ij} = \frac{1}{l_{ij}} \left(u_i^j - u_j^i \right) \tag{4.3}$$

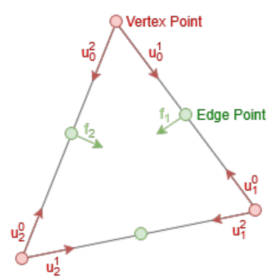

Figure 4.2 Face of the finite element with unknowns

Two facial unknowns f_1 and f_2 are added to two of the three edge points at one face. Contrary to the variables u_i^j, the facial unknowns f_i are only assigned locally at each element and do not cross boundaries. The purpose of the facial unknowns f is to provide a quadratic polynomial for the field component normal to the edges. This will lead to a linear approximation for the curl of the unknown vector field $\nabla \times \mathbf{u}$, providing sufficient accuracy. The overall vector field of this element is then calculated by a superposition of all nodes' vector attributions.

4.3 Solving the differential equation

A testing function $\mathbf{W}_n$ is defined, which is multiplied to Equation 4.1. Integrating over the whole test volume then leads to Equation 4.4. This yields N equations, with $n = 1, 2, ...N$, for each finite element in the domain Ω. This is a common procedure in FEM, and it works through orthogonalization of the residual of Equation 4.1 with respect to the function $\mathbf{W}_n$. This means the new goal of the solution is to minimize the residual by making $\mathbf{W}_n$ as orthogonal as possible [21].

$$\int_\Omega \left(\mathbf{W}_n \cdot \nabla \times \left(\frac{1}{\mu_r} \nabla \times \mathbf{E} \right) - k_0^2 \epsilon_r \mathbf{W}_n \cdot \mathbf{E} \right) \mathrm{d}V = 0 \tag{4.4}$$

Using the vector identity $\nabla \cdot (\mathbf{a} \times \mathbf{b}) = (\nabla \times \mathbf{a}) \cdot \mathbf{b} - \mathbf{a} \cdot (\nabla \times \mathbf{b})$ on Equation 4.4 provides a weak form of the equation, meaning a form of the original partial differential equation, which does not contain all original derivatives [6, 5]. Additionally, boundary terms come into play, as seen in the right hand side of the resulting Equation 4.5. The usefulness in this step has been described as lowering the highest-order derivative, therefore the approximating functions need to guarantee continuity of value, not of slope [11]. Another explanation is the possibility of incorporation of Neumann boundary conditions [21].

$$\int_\Omega \left[(\nabla \times \mathbf{W}_n) \cdot \frac{1}{\mu_r} \nabla \times \mathbf{E} - k_0^2 \epsilon_r \mathbf{W}_n \cdot \mathbf{E} \right] \mathrm{d}V = \underbrace{\oint_{\partial\Omega} \left(\mathbf{W}_n \times \frac{1}{\mu_r} \nabla \times \mathbf{E} \right) \cdot \mathrm{d}\mathbf{S}}_{\text{Boundary term}} \tag{4.5}$$

Next, the electric field $\mathbf{E}$ is represented by a superposition of basis functions. When applying Galerkin's method, the basis functions are equal to the test functions W_n. Equation 4.6 demonstrates the sum of the basis functions, which are weighted with the variable x_m. These variables x for all elements have to be solved, to find the electric field $\mathbf{E}$ over the whole domain. The FEM has therefore reduced the initial wave equation in Equation 4.1 to a simple linear matrix equation $Ax = b$, where A is a known $N \times N$ matrix, b contains port excitations and x is the unknown. Ideally, the basis functions are defined to be zero outside of their adjacent elements. This will result to zero for all entries in the matrix, where the test and basis function do not overlap. Therefore, the matrix is sparse, and will be solved much faster. In the end, other electromagnetic quantities can all be derived through the electric field.

$$\mathbf{E} = \sum_m^N x_m \mathbf{W}_n \tag{4.6}$$

Equation 4.7 shows what the matrix then looks like. Some manipulation on the boundary term have been made, so that it contains the surface impedance Z_s. The surface impedance defines the ratio of the electric field to the magnetic field on the boundary region. Furthermore, it contains the free space, which equals $\eta_0 \approx 377\,\Omega$.

$$A_{ij} = \int_\Omega \nabla \times \mathbf{W}_i \frac{1}{\mu_r} \nabla \times \mathbf{W}_j \,\mathrm{d}V - k_0^2 \int_\Omega \mathbf{W}_i \,\varepsilon_r \mathbf{W}_j \,\mathrm{d}V + \mathrm{i}k_0 \left(\frac{\eta_0}{Z_s} \right) \oint_{\partial\Omega} \mathbf{n} \times \mathbf{W}_i \cdot \mathbf{n} \times \mathbf{W}_j \,\mathrm{d}\mathbf{S} \tag{4.7}$$

4.4 Adaptive solution process

Each finite element therefore has a solved electric field assigned, which should approximate the real solution as closely as possible. To determine the error for each element, Equation 4.1 is evaluated. The elements with the highest residuals contain the largest deviation from the real result, meaning they have a large degree of error. Region in the mesh with large degrees of errors are refined, i.e. the tetrahedral finite elements are split into smaller ones. This allows the FEM solver to recalculate the fields in this region with higher precision, leading to a smaller residual. Consequently, the finite elements represent the fields more accurately, due to a smaller element size and higher resolution [4]. An additional method is increasing the order of the polynomial basis functions of elements with low degree of accuracy.

$$\nabla \times \left(\frac{1}{\mu_r} \nabla \times \mathbf{E}_{\text{solved}} \right) - k_0^2 \epsilon_r \mathbf{E}_{\text{solved}} = residual \tag{4.8}$$

To determine when the iterative refinement process is done and the solution good enough, some kind of threshold must be defined. One possibility is the Max ΔS parameter. It is compared to the difference of S-parameters of the defined excitation ports over two iterations. If, after a mesh refinement, the S-parameters of the ports do not significantly change anymore, meaning change less than Max ΔS, then the iterative process can be considered done. This described iterative process is shown in Figure 4.3.

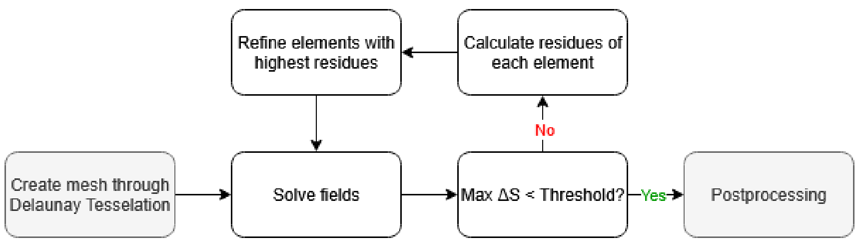

Figure 4.3 Adaptive solution process

Short HFSS introduction with boundary conditions, ports and modal and terminal solutions?

5 Numerical Investigations of Antennas in TEM Cells

5.1 Preliminary Considerations for Numerical Analysis

5.1.1 Skin Effect

The Skin-effect causes current to flow through a reduced area in a conductor, thus increasing resistance. The imaginary part κ of the complex wave number k is described by

$$\kappa = \omega \sqrt{\frac{\epsilon \mu}{2}} \left[\sqrt{1 + \left(\frac{\sigma}{\epsilon \omega} \right)^2} - 1 \right]^{1/2}. \tag{5.1}$$

The skin depth d is responsible for the increased conductor losses and is expressed as

$$d = 1/\kappa. \tag{5.2}$$

For highly conductive materials ($\sigma \ll \epsilon\omega$) the skin depth is $d \propto 1/\sqrt{\omega}$. Conductor losses P_{loss} are linearly proportional to the area of the conductor and therefore Skin-depth. They show the same dependency on the frequency $P_{\text{loss}} \propto 1/\sqrt{\omega}$ [9, p. 413]. Conductor losses contribute to the power consumption of the small loop antenna and is significantly larger than radiation power [2, p. 231].

The investigations in this thesis focus on the coupling behavior of antennas, including the radiation power consumed. All conducting surfaces in the simulation models are perfect electric conductors (PEC) to remove the impact of the Skin-effect.

5.1.2 Antenna models

Every antenna is fed with a round feedpoint, shown in Figure 5.1. They provide an incident wave of unit power (1 W). The antenna wires are modeled as PECs with a diameter of 0.2 mm. The geometry is intentionally kept simple, with the cylindrical wires pointing either in x-, y- or z-direction, without combining multiple orientations.

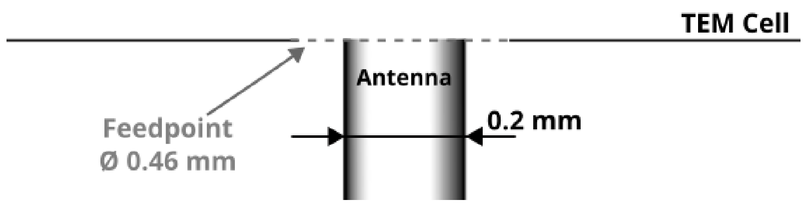

Figure 5.1 Geometry of an antenna's feedpoint used in simulation. The antenna is fed through a round waveport of diameter 0.46 mm. The antenna consists of PEC wire with diameter of 0.2 mm. This geometry leads to a reference impedance of $Z_0 \approx 50\,\Omega$.

5.1.3 TEM cell model

The TEM cell model used has a width of $a = 40$ mm, a height of $b = 24$ mm and a length of $l = 100$ mm, shown in Figure 5.2. The cell walls and septum are modeled as PECs. In the TEM cell simulation model, the tapered transition sections at the ports are omitted. This simplification allows unrestricted propagation of higher-order modes, facilitating investigations of their coupling behavior with antennas. The reference impedances of the output ports equal $Z_0 \approx 50\,\Omega$.

reference section where I discussed this

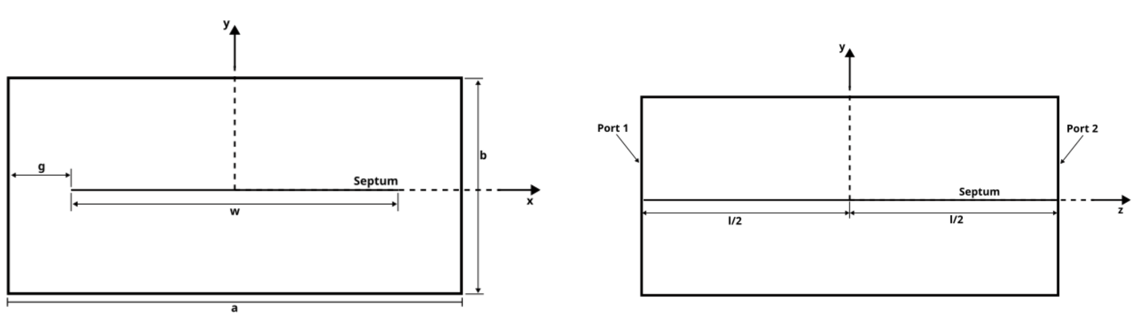

(a) xy-plane **(b)** yz-plane

Figure 5.2 Geometrical arrangement of the TEM cell used in simulations. The front shows the xy-plane, and the side the yz-plane of the TEM cell.

Upon exciting the output ports, the electric and magnetic energy W_e and W_m stored in the TEM cell is derived by Equation 2.23. The current and voltage at the output ports is found with Equations (5.7) to (5.8). The capacitance and inductance of the TEM cell are given by Equations (2.24a) to (2.24b). The reactance values fluctuate negligibly over frequency likely due to numerical inaccuracies. The average capacitance and inductance values over the frequency range are chosen. It is assumed that the TEM cell has a constant capacitance and inductance of $C_\mathrm{T} = 6.74\,\mathrm{pF}$ and $L_\mathrm{T} = 16.25\,\mathrm{nH}$.

5.1.4 Dipole moments models

A magnetic dipole moment can be expressed equivalently as either an electric current I_0 in a loop, or a magnetic current I_m in a line, as described in Equation 2.17. All dipole moments used in the simulations are assumed to be of infinitesimal length, as discussed in subsubsection 2.1.1 and subsection 2.2. For infinitesimal magnetic dipoles, Equation 2.17 simplifies to

$$|\mathbf{m}_\mathrm{m}| = j\omega\mu_0|\mathbf{m}_0|, \tag{5.3}$$

where $\mathbf{m}_\mathrm{m}$ with the unit Vm denotes the magnetic dipole moment in the magnetic current representation, and $\mathbf{m}_0$ with the unit Am^2 the moment in the electric current representation [16]. The simulation models represent magnetic dipole moments with $\mathbf{m}_\mathrm{m}$, which will be used in further investigations.

The electric and magnetic dipole moments are placed at the center of the TEM cell at $x = 0$, $y = b/2$, $z = 0$. As discussed in subsubsection 3.3.4, $\mathbf{e}^{\pm}_{\mathrm{TEM}}(x = 0, y = b/2, z = 0)$ has only a y-component at this location, while $\mathbf{h}^{\pm}_{\mathrm{TEM}}(x = 0, y = b/2, z = 0)$ has only an x-component. Consequently, the equivalent dipole moment $\mathbf{m}_\mathrm{e}$ is oriented along the y-direction, and $\mathbf{m}_\mathrm{m}$ along the x-direction.

Placing $\mathbf{m}_\mathrm{m}$ and $\mathbf{m}_\mathrm{e}$ in the center of the TEM cell therefore significantly simplifies modeling electrically small antennas with equivalent dipole moments. This assumption is valid for the TEM mode. This configuration is assumed for all numerical investigations following in this thesis, unless otherwise stated.

When normalizing to the free-space wave impedance Z_0, $\mathbf{m}_\mathrm{e}$ can be interchanged with an equivalent $\mathbf{m}_\mathrm{m}$ and vice-versa [12, p. 414]. Therefore, normalizing either $\mathbf{m}_\mathrm{e}$ or $\mathbf{m}_\mathrm{m}$ to the free-space wave impedance Z_0 enables a meaningful comparison between them.

All simulation results are counterchecked by inserting the equivalent dipole moments into the TEM cell and comparing the power and phase at the output ports with the antenna's results.

Figure 5.3 demonstrates the normalized output power of an electric dipole moment pointing in y-direction, and one in z-direction. This simulation only demonstrates the coupling behavior of the dipole moments over frequency, to explain the non-linear coupling of certain antennas. If dipole moments in certain positions and orientations couple with a different proportionality than the standard two dipole moments (ez and my), then the non-linear coupling may be explained that way.

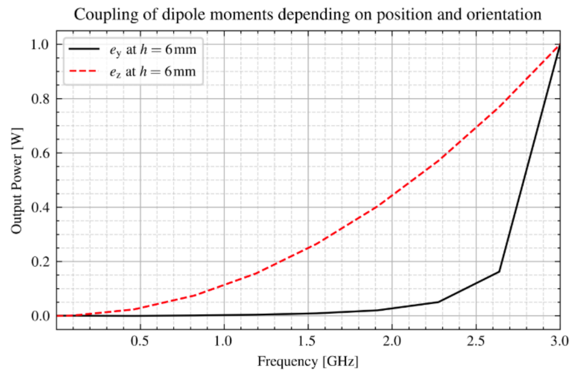

Figure 5.3 Comparison of normalized output power of electric dipole moments

The electric dipole moment in z-direction e_z demonstrates the expected behavior: As the frequency rises, this dipole moment rises linearly and thus increases the output power quadratically. The electric dipole moment in y-direction e_y also increases linearly increase with frequency, but does not significantly change the output power for the low frequencies. However, as the frequency approaches the cut-off frequency of the next-higher order mode, the coupling rises significantly.

This simulation is repeated where the dipole moments are located at a height of $h = 6$ mm, which is the dead center of the TEM cell, and $h = 9$ mm, which is near the top wall of the TEM cell. The simulation results are similar for both cases.

Most importantly, this simulation shows that the dipole moments have a relation to the frequency independent on their position. While their magnitude themselves do depend on the position, the relation to the frequency does not.

An electric dipole in direction of propagation lead to no power transfer, even in higher order modes. That's because these fields do not overlap with the dipole, for which TM modes would be necessary.

Repeat Simulation for several other dipole moment positions and orientations?

As show in the previous simulations, antennas may be represented by dipole moments. This can be done in simulation models, which would otherwise be computationally too effortful. The dipole moments may be put into a shielded enclosure around a larger electronic system, as has been done in [18].

5.1.5 Mesh modifications

The mesh determines the resolution of the field quantities over the computational domain. Since electrically small conductors are involved, implementing small mesh elements in their proximity is necessary for accurate modeling of near-fields. Adaptive meshing algorithms may neglect this task, due to the low impact of these near-fields on the solution of the overall computational domain. Consequently, adjusting mesh element sizes does not significantly influence the overall solution of the model, but greatly improves the accuracy of near-field investigations.

The maximum mesh element length in error-prone volumes are adjusted, until the obtained results show a reasonably low amount of numerical artifacts. Such volumes are commonly located adjacent to feedpoints and along edges of small conductors, where large field intensities occur within small spatial regions. The simulation models used in this thesis use roughly 15 elements on the surfaces of such critical volumes to achieve a reasonable representation of these regions while avoiding excessively large meshes.

5.1.6 S-parameters and derived data

The TEM cell with an antenna is modeled as a three-port network. The two output ports of the TEM cell are denoted as ports 1 and 2, while the antenna feedpoint is marked as port A. The behavior of this system is fully characterized by its scattering matrix, given as

$$[S] = \begin{bmatrix} S_{11} & S_{12} & S_{1A} \\ S_{21} & S_{22} & S_{2A} \\ S_{A1} & S_{A2} & S_{AA} \end{bmatrix}. \tag{5.4}$$

The coupling between the antenna and the two ports of the TEM cell are described by S-parameters, specifically the forward transmission coefficients S_{A1} and S_{A2}. The phases of the forward transmission coefficients Φ_{A1} and Φ_{A2} provide information on the phase shift between the incident wave at port A, and the transmitted wave at output ports 1 and 2. The magnitude of this coefficient is the same for the antenna to both ports $|S_{\mathrm{A1}}| = |S_{\mathrm{A2}}|$, given that the antenna is placed far from the output ports. The power transferred from the antenna P_{A} to the output ports P_1 and P_2 is derived through

$$P_{\mathrm{A}} = \frac{P_1}{10^{|S_{\mathrm{A1}}|/10}} = \frac{P_2}{10^{|S_{\mathrm{A2}}|/10}}. \tag{5.5}$$

Consequently, if the normalized electric field distribution of the TEM mode $\mathbf{e}^{\pm}{}_{\mathrm{TEM}}$ is unknown, it may be derived by setting the output power of a waveport to $P_1 = P_2 = 1/2\,\mathrm{W}$. For example, the uniformly distributed, normalized electric field of the TEM mode along the y-axis at the center of the TEM cell ($z = 0$, $x = 0$) is derived by

$$|a_{\mathrm{TEM}}| \cdot \mathbf{e}^{+}_{\mathrm{TEM}}(x = 0, y, z = 0) = \frac{\sqrt{P_1 Z_0}}{b/2}. \tag{5.6}$$

The difference in phase of S_{A1} and S_{A2} influences the magnitude of magnetic dipole moments and electric dipole moments, as discussed in subsubsection 3.4.2. The peak value of the current through the feedpoint of the antennas is calculated with the S-parameters,

$$I_{\mathrm{A}} = \sqrt{2P_{\mathrm{A}}}\frac{(1 - S_{\mathrm{AA}})}{\sqrt{Z_0}}. \tag{5.7}$$

P_{A} is the incident power wave applied to the port. The peak voltage at the feedpoint is calculated in a similar fashion as

$$V_{\mathrm{A}} = \sqrt{2P_{\mathrm{A}}}(1 - S_{\mathrm{AA}})\sqrt{Z_0}. \tag{5.8}$$

Another method to derive voltages and currents is by integration of field intensities. Special care has to be taken at mesh refinement in the area of integration to reduce numerical errors.

The impedance seen from the antenna feedpoint is

$$Z_{\mathrm{A}} = Z_0 \frac{1 + S_{\mathrm{AA}}}{1 - S_{\mathrm{AA}}}. \tag{5.9}$$

All values are peak values, unless otherwise stated.

5.1.7 Investigation of field regions

Update field plots

In this section, the coupling-field regions described in subsection 2.4 are analyzed using the model shown in Figure 5.4. This analysis examines whether frequency-dependent coupling behavior of the TEM cell can be attributed to changes in the dominant coupling-field region.

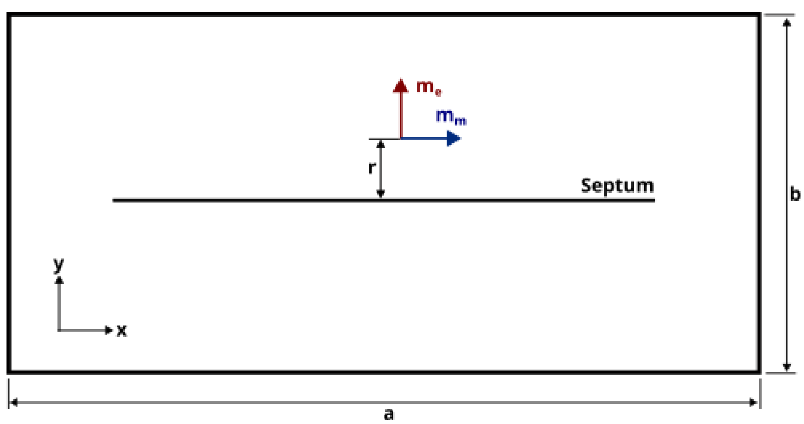

Figure 5.4 A TEM cell containing an electric $\mathbf{m}_{\mathrm{e}}$ and a magnetic dipole moment $\mathbf{m}_{\mathrm{m}}$ in the center $x = 0, y = r = b/4, z = 0$ to investigate the field regions in which the coupling occurs.

To determine the influence of the field regions on the coupling effect, $\mathbf{m}_{\mathrm{e}}$ and $\mathbf{m}_{\mathrm{m}}$ are placed in two different TEM cells of dimensions $a = 10\,\mathrm{mm}, b = 6\,\mathrm{mm}$ and $a = 40\,\mathrm{mm}, b = 24\,\mathrm{mm}$. The $k \cdot r$-factor for both cases is shown in Figure 5.5.

aking the TEM cell smaller such that $k \cdot r \ll 1$, proves to be feasible. The following simulations are conducted with a TEM cell of dimensions $a = 10\,\mathrm{mm}$ and $b = 6\,\mathrm{mm}$, visible in Figure 5.4.

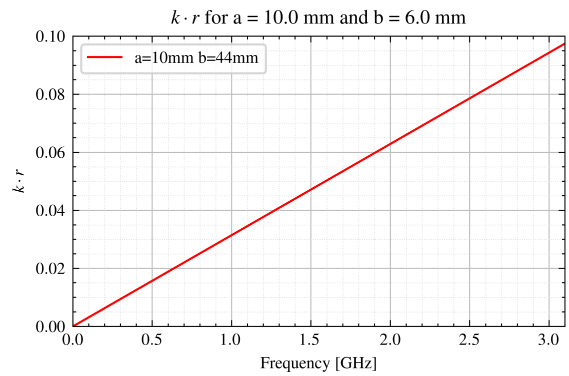

Figure 5.5 $k \cdot r$ in small TEM cell

First, the current loop antenna used in subsection 5.3 is placed in the dead center of the TEM cell. The equivalent dipole moments are shown in Figure 5.6. In the Figure 5.7 next to it, the dipole moments of the same antenna in the larger TEM cell used before ($a = 40$ mm and $b = 24$ mm) are presented.

TODO:Redo plots

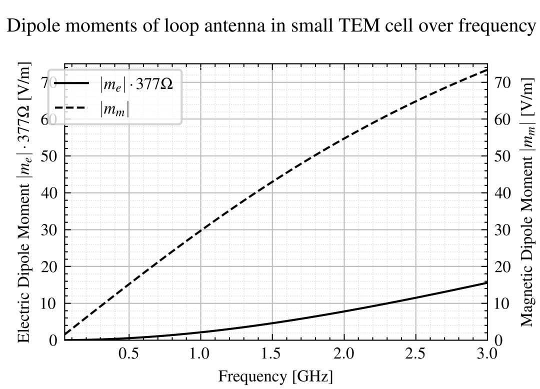

Figure 5.6 Moments in small TEM cell

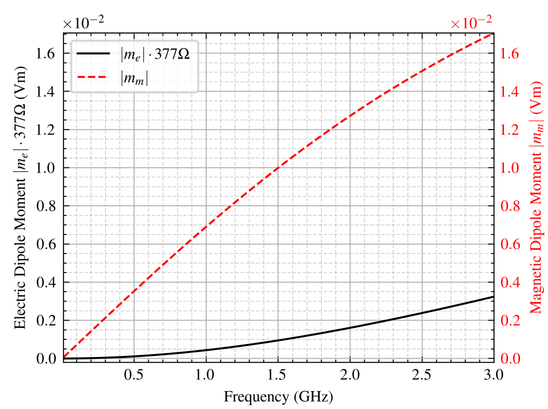

Figure 5.7 Moments in normal TEM cell

This is done to compare the dipole moments in both cases. While they clearly increased by magnitude in case of the small TEM cell due to better coupling, their non-linear frequency relation still remains. This means that the change of field regions is not the reason for this behavior.

The $k \cdot r$ factor is determined in Figure 5.5 in the frequency range from 1 MHz to 3 GHz for the small TEM cell. This factor does not surpass 0.1, thus fulfilling the requirement $k \cdot r \ll 1$ for this investigation. For comparison, the $k \cdot r$ factor over a wider frequency range are shown in Figure 5.5 for the normal sized TEM cell ($a = 40$ mm and $b = 24$ mm) and a degenerately high TEM cell ($a = 10$ mm and $b = 44$ mm). The high TEM does not have a port impedance of $50\,\Omega$, and is an attempt to achieve a large $k \cdot r$ factor without

TODO: Insert kr, describe where r is measured, describe why the suspicion was that kr could influence this and higher-order modes propagating. The markers in **??** indicate the cut-off frequency, in which the next higher-order mode propagates. They demonstrate, that even in the high TEM cell a $k \cdot r = 1$ is not achieved.

Fix figures: Titles and Legends. Add kr of normal cell.

Now, three simulations are conducted with different excitation sources in the small TEM cell:

- The current loop
- The equivalent dipole sources e_z and m_m of the current loop
- The equivalent magnetic dipole source m_m, neglecting e_z

Figure 5.8 shows the output power over frequency normalized to 1 W for all three constellations. The normalization is done to qualitatively discuss the frequency-dependent coupling behavior. Figure 5.9 demonstrates the phase shift between the powers at the two waveports over frequency.

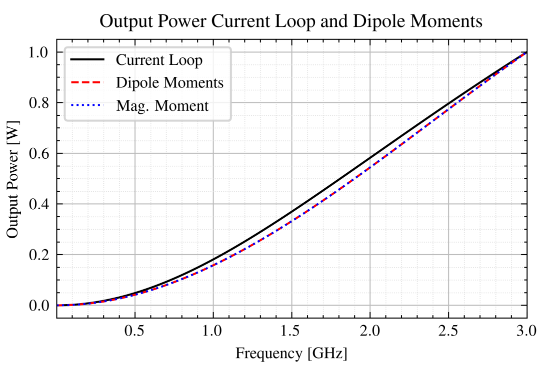

Figure 5.8 Output powers

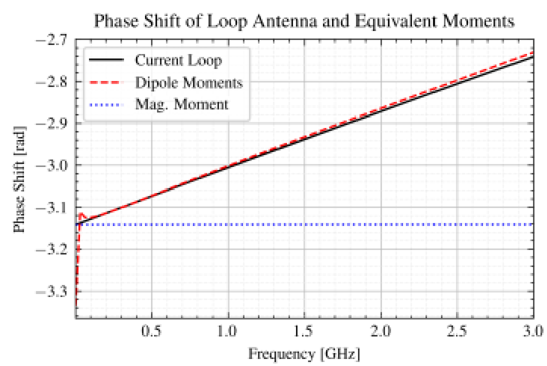

Figure 5.9 Phase shifts

The frequency dependent behavior of the output power does not change depending on the type of dipole moment used. This is significant, because this shows that the dipole moments do not exhibit different coupling behaviors in the TEM cells. This is further proven in the phase shift plots. The magnetic dipole moment causes a constant phase shift of $-\pi$. If this was not the case, this would mean that the coupling behavior of the magnetic dipole moment in the TEM cell would change. Since the opposite is the case, this poses as good evidence against arguments of change in field regions causing the non-linear dipole moment behavior. Instead, it is very likely to be caused by the geometry of the antenna.

5.2 Monopole Antenna

5.2.1 Setup

The monopole antenna shown in Figure 5.10b is installed in the TEM cell and connected to a feed point located on the top wall. The current flowing through it is aligned with the TEM mode and produces an electric dipole moment.

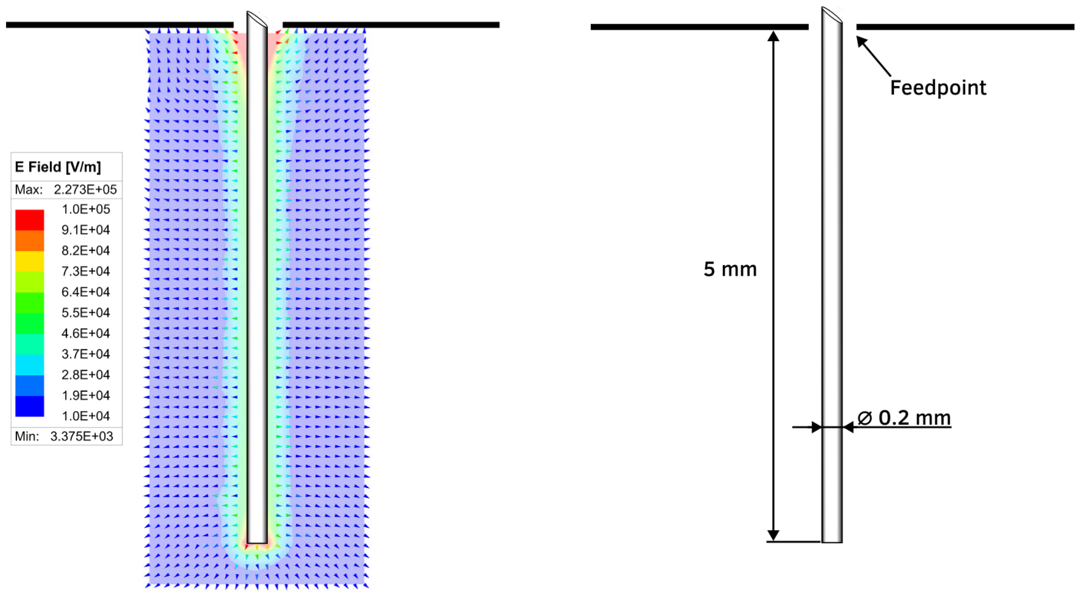

(a) The numerically derived near-field plot of the monopole antenna shows strong displacement currents near the feedpoint and at the wire end. Simulation results are improved by decreasing mesh element lengths in these regions.

(b) The geometrical aspects of the cylindrical monopole antenna, as implemented in the simulation model.

Figure 5.10

The antenna has a physical length of 5 mm, making it electrically short for frequencies up to 6,GHz. For frequencies up to 1.25 GHz, it can be accurately approximated as an infinitesimal electric dipole, as discussed in subsubsection 2.1.1. At higher frequencies, up to 6,GHz, it behaves as a small electric dipole, as explained in subsubsection 2.1.2.

5.2.2 Equivalent dipole moments

The corresponding equivalent electric and magnetic dipole moments, $\mathbf{m}_e$ and $\mathbf{m}_m$, are analytically derived using Equations (3.36) to (3.37). The resulting $\mathbf{m}_e$ shown in Figure 5.11 increases approximately linearly over frequency, while the magnetic dipole moment is negligible over the whole frequency range.

Furthermore, the phase difference between the power at the two output ports is zero across the entire frequency range. This observation is consistent with the assumption that a pure electric dipole moment introduces no phase shift between the output port powers, as discussed in subsubsection 3.4.2.

5.2.3 Electrical characteristics

The feedpoint voltage V of the antenna, shown in Figure 5.12a, remains largely constant over the investigated frequency range. Consequently, the voltage induced between the

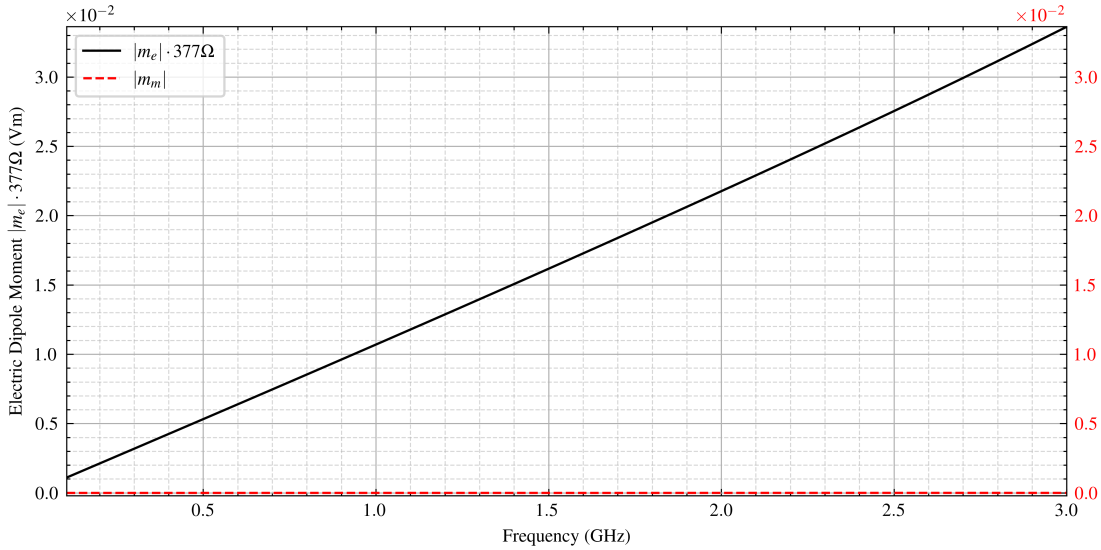

Figure 5.11 The equivalent electric and magnetic dipole moments analytically calculated with Equations (3.36) to (3.37). To enable direct comparison with the magnetic dipole moment, the electric dipole moment is normalized by the impedance of free space Z_0, as discussed in subsubsection 5.1.4.

antenna and the septum is negligible. This observation is consistent with the absence of a magnetic dipole moment $\mathbf{m}_m$, which is directly related to the induced voltage according to Equation 3.41.

The feedpoint current I, shown in Figure 5.12a, increases linearly. The entire current contributes to displacement currents due to the absence of a return path. According to Equation 3.47, $\mathbf{m}_\mathrm{e}$ is proportional to the displacement current to the septum. The linear increase of $\mathbf{m}_\mathrm{e}$ and I are therefore related.

At low frequencies, the antenna impedance in Figure 5.12b shows a high magnitude, which rapidly decreases as frequency increases. Over the whole frequency range, it exhibits highly capacitive behavior, which is consistent with Equation 2.10 and the discussion in subsubsection 2.1.1.

Applying Equation 3.47 to determine $\mathbf{m}_\mathrm{e}$ requires knowledge of the magnitude of the displacement current to the septum. Another possibility of determining $\mathbf{m}_\mathrm{e}$ is the integration of the current I weighted by $\mathbf{e}^{\pm}_{\mathrm{TEM}}$ along the monopole antenna, as given in Equations (3.39a) to (3.39b). At a frequency of 3,GHz, this approach yields

$$\mathbf{m}_\mathrm{e}(f = 3\,\mathrm{GHz}) = \int_{b/2-5\,\mathrm{mm}}^{b/2} I(y, f = 3\,\mathrm{GHz})\,dy = 85.69\,\mu\mathrm{Am} \cdot \hat{\mathbf{a}}_z, \tag{5.10}$$

which corresponds to $\mathbf{m_e} \cdot Z_0 = 3.23 \cdot 10^{-2} \cdot \mathrm{Vm}\,\hat{\mathbf{a}}_z$ when normalized by the free-space wave impedance Z_0. This approximates $\mathbf{m}_\mathrm{e}$ in Figure 5.11 at 3 GHz reasonably well, therefore supporting Equations (3.39a) to (3.39b).

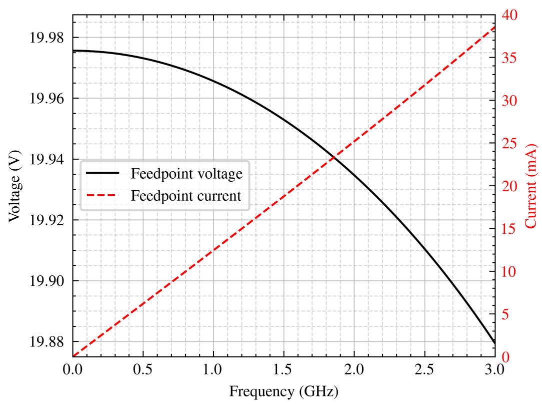

(a) Magnitude of the voltage and current applied at the feedpoint of the monopole antenna over frequency, derived through the S-parameters with Equations (5.7) to (5.8).

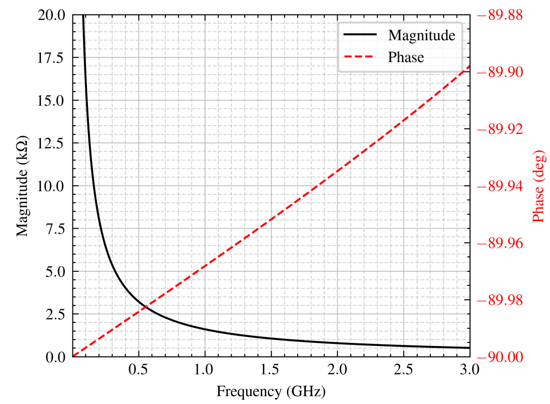

(b) Magnitude and phase of the antenna impedance over frequency, derived through the S-parameters with Equation 5.9.

Figure 5.12

The derived equivalent dipole moments $\mathbf{m}_e$, $\mathbf{m}_m$ in the TEM cell produce the output power over frequency shown in Figure 5.13b, where they are compared with the output power produced by the monopole antenna. The equivalent dipole moment approximation of the monopole antenna loses precision when approaching the cut-off frequency of the first higher-order mode TE_{01}. Considering the coefficients a_{TE01} and b_{TE01} of the TE_{01}-moment increases accuracy, which is not done here.

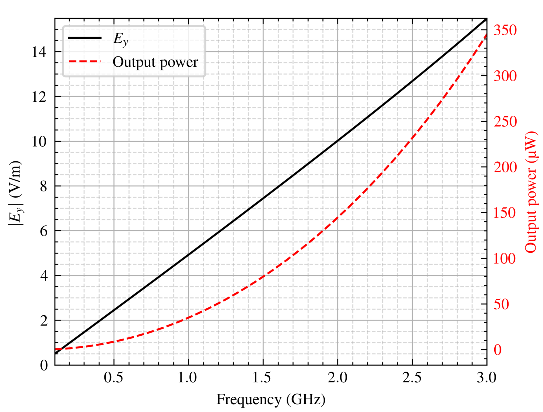

(a) Electric field in y-direction E_{y} at $x = 0, y = b/4, z = \pm l/2$, and power at one output port, derived with the S-parameters in Equation 5.5.

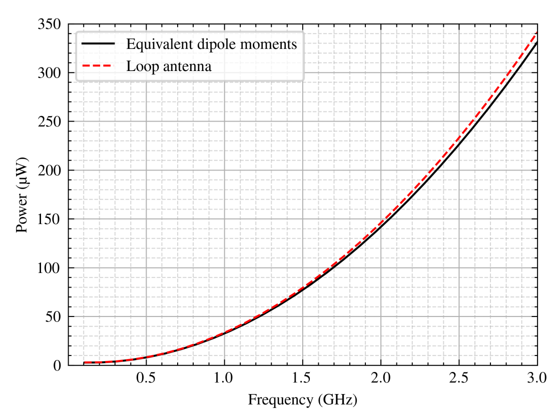

(b) Comparison of output power produced by the monopole antenna and its equivalent dipole moments to demonstrate validity of the model.

Figure 5.13

The distribution of the current along the monopole antenna shown in Figure 5.16 is numerically derived by integrating the magnetic field intensity in a closed loop around the wire using Ampère's law,

$$\oint_{\mathbf{l}} \mathbf{H} \cdot d\mathbf{l}' = I. \tag{5.11}$$

A fine mesh resolution, as discussed in subsubsection 5.1.5, is important for accurate results delivered by Equation 5.11.

Near the feedpoint at 0 mm non-linear behavior becomes apparent due to significant displacement currents and numerical artifacts in this region. This causes the current to exhibit a steeper decline with non-physical oscillations.

The current distribution at 3 GHz (see Figure 5.14) approximates that of a small electric dipole, as described in subsubsection 2.1.2. It shows an approximately linear decrease towards zero.

The current distribution at 1 MHz, shown in Figure 5.15, also decreases linearly along the monopole antenna. I can be approximated with an infinitesimal electric dipole, as discussed in subsubsection 2.1.1.

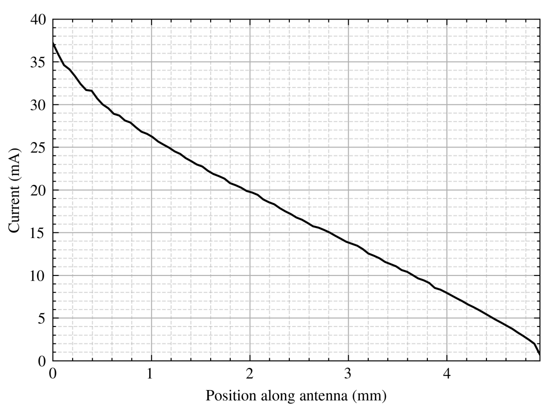

Figure 5.14 The current distribution along the monopole antenna at 3 GHz shows a linear decrease, which is common for a small electric dipole.

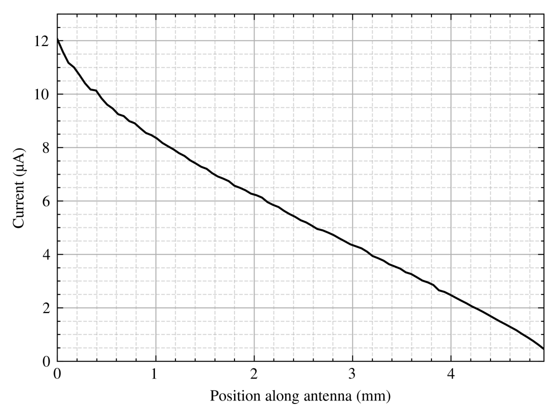

Figure 5.15 The current distribution along the monopole antenna at 1 MHz shows a large decline near the feedpoint due to increased displacement currents. It then approaches a roughly constant current distribution, which is typical for an approximate infinitely small electric dipole.

Figure 5.16

TODO: Equivalent circuit for Monopole Antennas

An equivalent circuit is derived in Figure 5.17, which is known as Chu equivalent circuit for a short dipole [10].

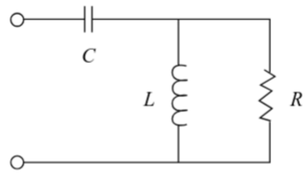

Figure 5.17 The Chu equivalent circuit for a short electric dipole models the monopole antenna's behavior.

5.2.4 Current distribution on septum

Figure 5.18a shows the surface current density on the septum induced by the monopole antenna at 3 GHz. The current reaches both output ports in phase, confirming the absence of a phase shift between the output port powers.

Figure 5.18b shows the current density of the septum at 3.3 GHz, with the TEM-mode compensated at the output ports. Due to the magnetic fields propagating in the z-direction, the current on the septum creates a pattern of swirls. Furthermore, the phase shift of the induced power between the output ports is π. This results from the magnetic field intensities of the TE_{01}-mode being in-phase at the output ports, opposed to the magnetic field intensities of the TEM-mode.

idea: offset in z-direction, show surface current how it gets a pahse shift at waveports, and a magnetic dipole moment appears to be induced

idea: offset in x-direction, showing surface current and explaining the decrease in power transfer (normal E-field distribution)

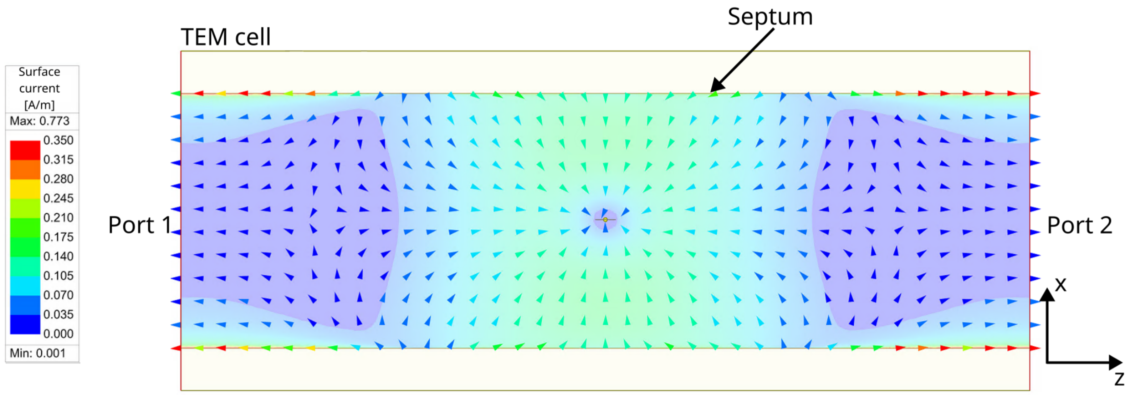

(a) Current surface density at 3 GHz, where mostly the TEM-mode propagates.

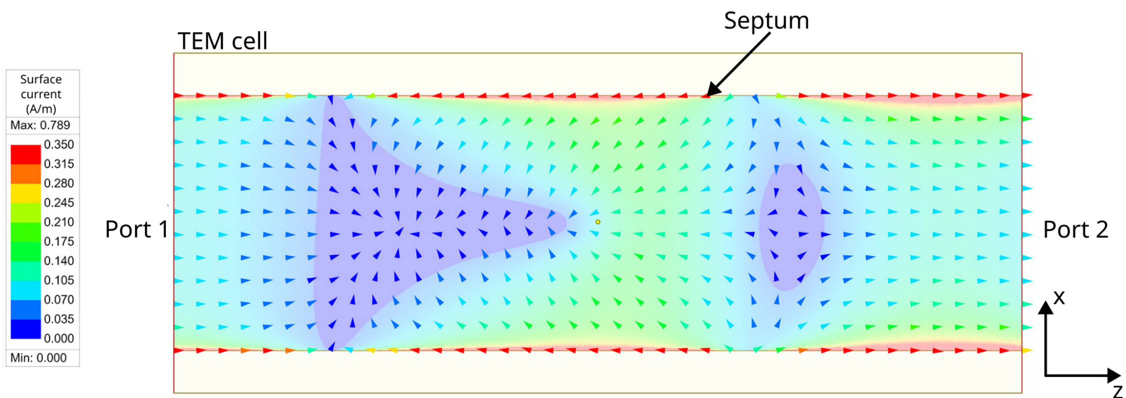

(b) Current surface density of only the TE_{01}-mode at 3.3 GHz with the TEM mode compensated.

Figure 5.18 Current surface densities at different frequencies, below and above the cut-off frequency of the TE_{01}-mode.

5.2.5 Electromagnetic energy in the TEM cell

The monopole antenna generates electromagnetic fields within the TEM cell, resulting in stored electromagnetic energy. The frequency-dependent electric energy is shown in Equation 2.23. Its quadratic increase correlates with the output power in Figure 5.13a. The corresponding magnetic energy is several orders of magnitude smaller due to the capacitive behavior of the monopole antenna and is therefore neglected. From the stored electric energy, both the real and imaginary components of the power consumed by the antenna can be determined.

Moreover, the effective inductance and capacitance of the monopole antenna inside the TEM cell can be derived from the magnetic and electric energy expressions given in Equations (2.24a) to (2.24b). Using the peak value of the electric energy shown in Figure 5.19, the capacitance is estimated to be $C \approx 108.55\,\mathrm{fF}$.

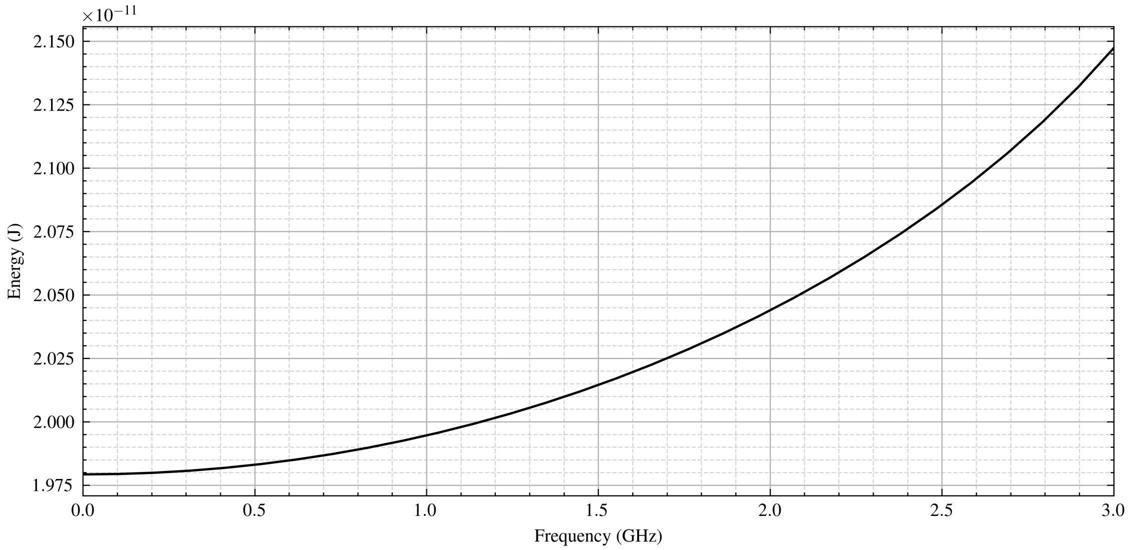

Figure 5.19 Electric energy determined by integrating the electric field over the TEM cell volume, using Equation 2.23.

5.3 Loop antenna

5.3.1 Setup

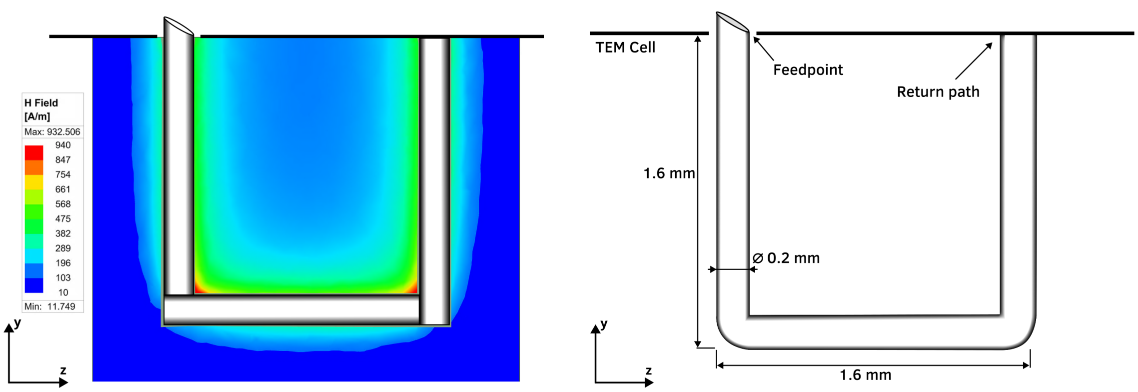

(a) TODO: Maybe show E-Field instead

(b) The geometry of the loop antenna assimilates a square with round edges. Each side has a length of 1.6 mm. The return path leads back to the PEC surface of the TEM cell.

Figure 5.20

A square loop antenna is placed in the center of the TEM cell. It consists of four wires with a length of 1.6 mm each, and it is electrically short for frequencies up to 4.69 GHz. The square geometry is preferable to a round version in the numerical simulations, as it allows for more accurate meshes and enables a clearer investigation of the resulting dipole moments.

The normal vector of the loop surface points in x-direction, leading to a maximum coupling with the magnetic field of the TEM-mode. In contrast to the monopole antenna discussed in subsection 5.2, a return path for the current exists, which generates a magnetic dipole moment.

5.3.2 Equivalent dipole moments

The equivalent dipole moments of the loop antenna are plotted in Figure 5.21a. The magnetic dipole moment $\mathbf{m}_\mathrm{m}$ dominates over the electric dipole moment $\mathbf{m}_\mathrm{e}$. Opposed to the case of a monopole antenna, $\mathbf{m}_\mathrm{e}$ and $\mathbf{m}_\mathrm{m}$ demonstrate non-linear behavior over frequency, which is investigated further in subsubsection 5.3.3.

Furthermore, the phases of the powers at the output ports, shown in Figure 5.21b, differ from one another. The phase shift in the low-frequency range approaches π, but gradually decreases with increasing frequency. This agrees with the analysis presented in subsubsection 3.4.2, which predicts a phase shift of π when only $\mathbf{m}_\mathrm{m}$ is present, and a reduced phase shift as $\mathbf{m}_\mathrm{e}$ increases, as is the case here.

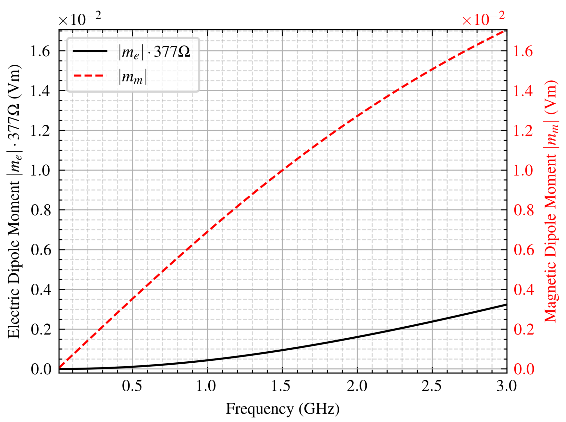

(a) The equivalent dipole moments of the loop antenna derived analytically with Equations (3.36) to (3.37). The electric dipole moment $\mathbf{m}_\mathrm{e}$ is weighted with Z_0 to enable comparison with $\mathbf{m}_\mathrm{m}$.

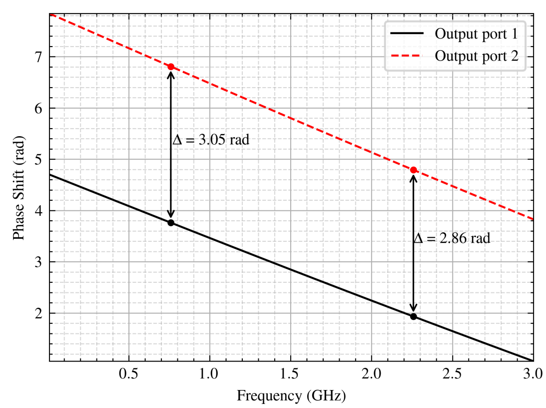

(b) Phases of the powers at output ports 1 and 2, derived from the S-parameters, as discussed in subsubsection 5.1.6. The analysis focuses on the phase shift between the two ports, which provides information about the presence of $\mathbf{m}_\mathrm{m}$ and $\mathbf{m}_\mathrm{e}$, as investigated in subsubsection 3.4.2.

Figure 5.21

TODO: Redo magnetic and electric energy plots logarithmic. Check feed and return current.

The power and E_y induced by the loop antenna at the output ports is shown in Figure 5.22a, and increases not as steeply as the output power of the monopole antenna exhibited in Figure 5.13a. This directly correlates with the decrease of $\mathbf{m}_\mathrm{m}$ with increasing frequency.

Figure 5.22b demonstrates the output power generated by the equivalent dipole moments $\mathbf{m}_\mathrm{m}$, $\mathbf{m}_\mathrm{e}$ and the loop antenna. Their similarity support the validity of the model used.

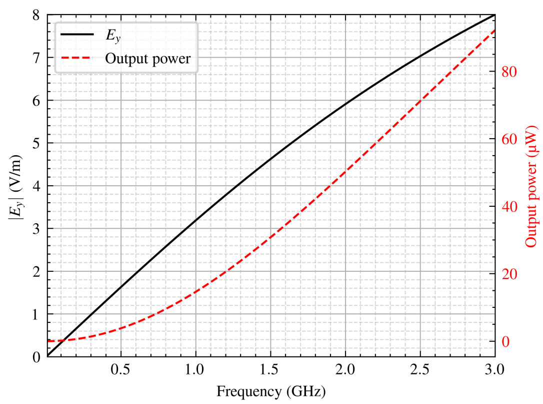

(a) Electric field in y-direction E_{y} at $x = 0, y = b/4, z = \pm l/2$, and power at one output port, derived with the S-parameters in Equation 5.5.

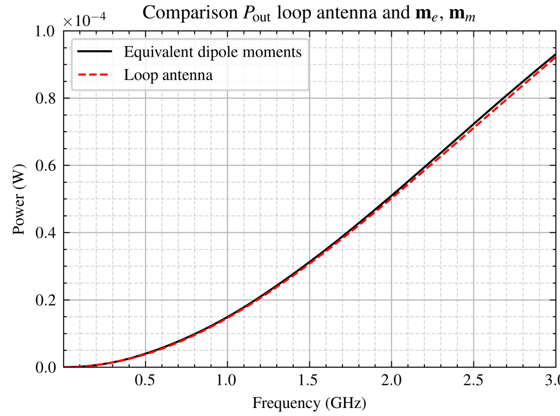

(b) Comparison of output power produced by the monopole antenna and its equivalent dipole moments.

Figure 5.22

5.3.3 Electrical characteristics

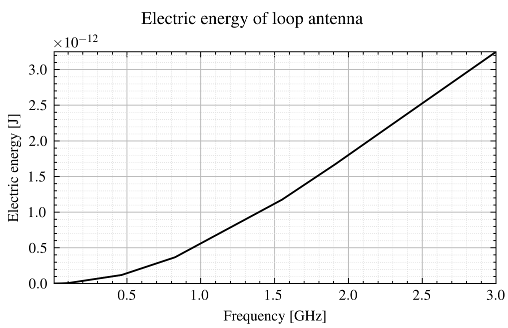

(a) Electric energy

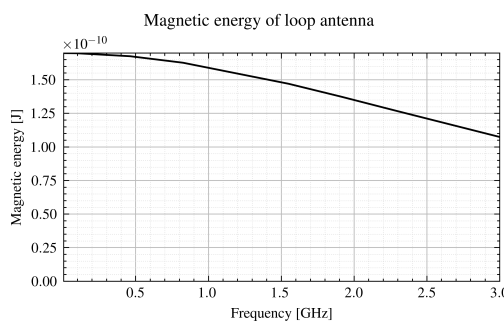

(b) Magnetic energy

Figure 5.23

The current I in the loop antenna changes along the antenna wire as shown in Figure 5.24a, indicating displacement current coupling to the septum and back to the feedpoint. The difference between the feedpoint and return path current increases over frequency, translating to rising displacement currents. Furthermore, the decrease in feed current over rising frequency, shown in **??**, also hints to the presence of increasing displacement currents. Consequently, $\mathbf{m}_e$ gains a significant magnitude according to Equation 3.47, influencing the electric coupling behavior of the antenna.

The feedpoint current is derived through integration of $\mathbf{H}$ in a closed loop of radius 0.11 mm, measured 0.17 mm above the feedpoint. The return path current is processed with the same loop integration at the same height above the PEC surface. The results vary with height above the PEC surface due to the displacement currents in the near-field.

Insert free-space PEC loop simulations.

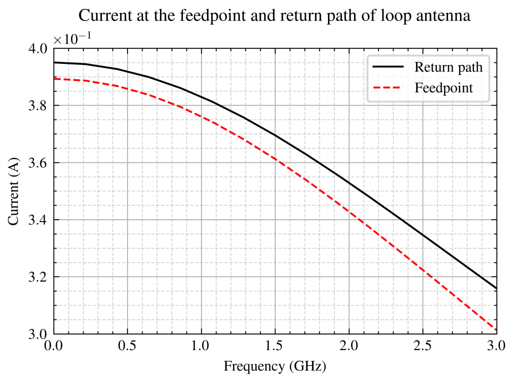

(a) The current at feedpoint and return path of the loop antenna demonstrates an increasing difference with frequency, indicating a growing occurrence of displacement currents. It is determined with Equation 5.11.

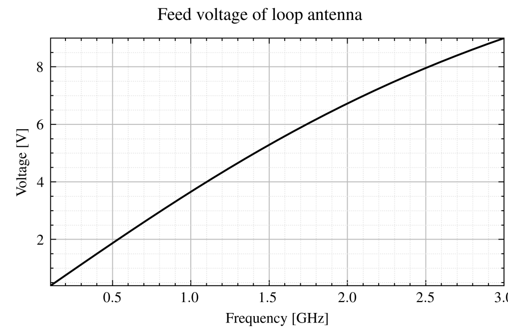

(b) The voltage across the feedpoint, which is determined with Equation 5.8.

Figure 5.24

Figure 5.24b demonstrates the voltage at the feedpoint of the antenna, which significantly rises over the frequency, signaling increased induced voltage V_n. According to Equation 3.41, this directly correlates with $\mathbf{m}_\mathrm{m}$, which also becomes apparent when comparing their behavior shown in Figures 5.21a to 5.24b.

The increase in voltage also correlates with the displacement current. It raises the potential on the loop antenna, therefore increasing the charge distributions and displacement currents.

todo: replace effective voltage and current with peak values for consistency.

The increases in voltage and decrease in current follows from the impedance, depicted in Figure 5.25. The loop antenna shows strongly inductive behavior.

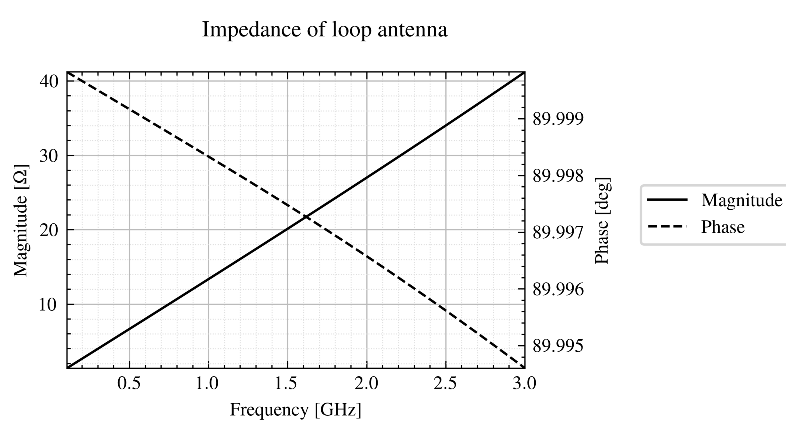

Figure 5.25 Magnitude and phase of the impedance of the current loop antenna.

5.3.4 Equivalent circuit model

A better understanding and an useful model for calculations is an equivalent circuit model. Figure 5.26a demonstrates an equivalent circuit for the electrically small loop antenna, where C models stray capacitances, R_L the losses, R_r the radiation, L_i the internal inductance and L_A the external inductance [2, p. 244]. The model used in the simulation consists of a perfect conductor, therefore R_L and L_A are neglected. Instead, the simplified schematic in Figure 5.26b is used, where R_A, L_A and C_A model the impedance behavior of the antenna.

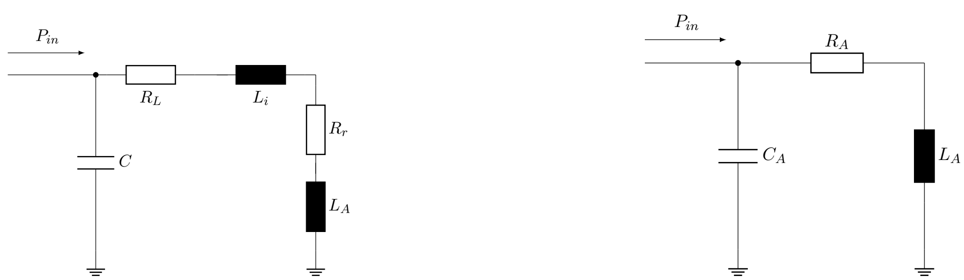

(a) Full equivalent circuit **(b)** Reduced equivalent circuit

Figure 5.26 Equivalent circuits of the small loop antenna.

The antenna is placed on a PEC surface in an open space. The inductance and capacitance are derived according to **??**, in the case of the circuit in Figure 5.26b this leads to

sketch

$$L = 2\frac{W_m}{I_{in}^2} = \frac{V_{in}^2}{2\omega^2 W_m}, \tag{5.12a}$$

$$C = \frac{2W_c}{V_{in}^2}. \tag{5.12b}$$

Plot inductance and capacitance

In the investigated frequency range, the inductive impedance is significantly smaller than the capacitive impedance, resulting in a predominantly inductive antenna behavior. The model further demonstrates, that the input voltage increases over frequency, therefore increasing the voltage drop across the capacitor. Physically, this corresponds to increased displacement current and electric coupling.

The result cross-checked with

$$L_A = \frac{2\mu_0 l}{\pi}\left[\ln\left(\frac{l}{w_r}\right) - 0.774\right], \tag{5.13}$$

which is an approximation of the inductance of a square current loop in free-space [2, p. 245]. There, l is the length of one side of the antenna, and w_r is the wire radius. Equation 5.13 yields $L = 2.32\,\mathrm{nH}$ for the loop antenna in investigation.

The model is extended in Figure 5.27 with an equivalent circuit of the TEM cell, which consists of an equivalent inductance $L_T = L_{T1} + LT2$ and capacitance $C_T = C_{T1} + C_{T2}$. After checking the frequency range in which the equivalent circuit of the TEM cell is valid, it is connected with the circuit of the antenna with C_k, which models the coupling through displacement current, and the mutual inductances $M_{A,T1}$ and $M_{A,T2}$, which correspond to coupling through induced voltages. The mutual inductances are given as

$$\mathbf{V} = j\omega \begin{bmatrix} L_A & M_{A,T1} & M_{A,T2} \\ M_{T1,A} & L_{T1} & 0 \\ M_{T2,A} & 0 & L_{T2} \end{bmatrix} \mathbf{I}. \tag{5.14}$$

Due to the modeling of the power transfer with C_k, $M_{A,T1}$ and $M_{A,T2}$, the radiation resistance of the antenna shown in Figure 5.26b is neglected.

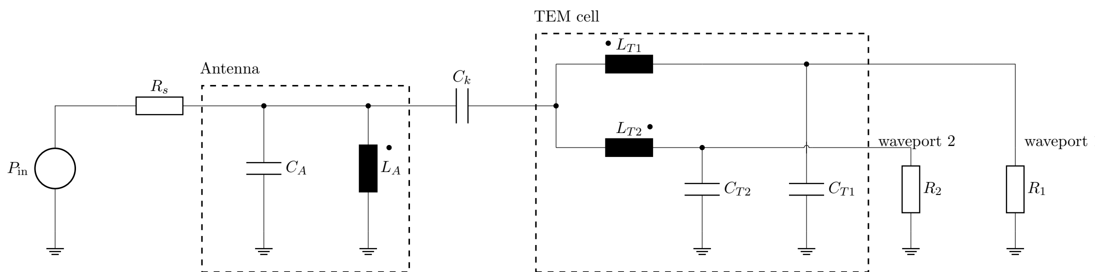

Figure 5.27 Circuit representing the TEM cell, small loop antenna and their coupling.

The magnetic dipole moment $\mathbf{m}_m$ is derived by the induced voltage in L_T1 and $LT2$ according to Equation 3.41, and the electric dipole moment $\mathbf{m}_e$ by the displacement current in C_k through Equation 3.47. This leads to $\mathbf{m}_e$ and $\mathbf{m}_m$ depicted in Figure 5.28, which qualitatively agree with the dipole moments of the loop antenna, but deviate in value by up to 15 %.

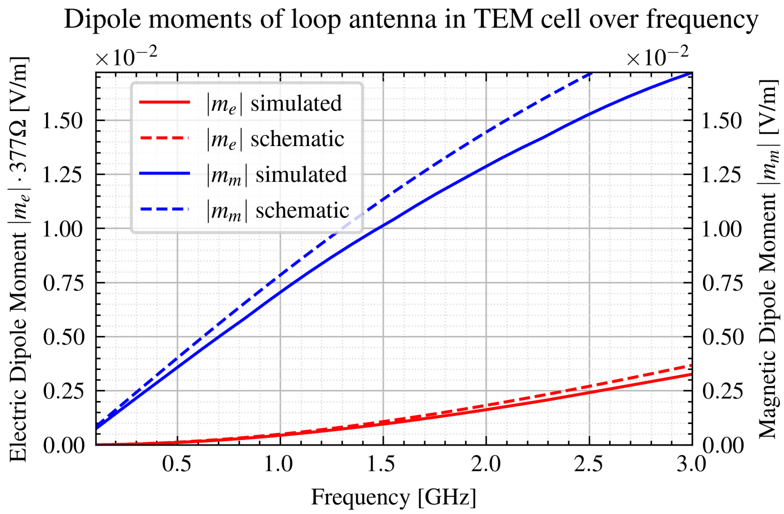

Figure 5.28 Equivalent dipole moments derived by the equivalent circuit compared to the dipole moments of the loop antenna in Figure 5.21a.

5.3.5 Current distribution on septum and higher order modes

The loop antenna generates a current on the septum of the TEM cell, as shown in Figure 5.29. At a frequency of 3 GHz, the current arrives at the output ports out of phase, as visible in Figure 5.29a. This agrees with **??**, which predicts a 180°phase shift in case of a pure magnetic dipole moment.

TODO: log scale in Figure 5.30. Broader frequency range.

When the position of the current loop antenna is rotated by 90°and contains an offset of $x = 7\,\text{mm}$, the transmission of power is not possible. As visible in the current distribution Figure 5.29b, there is no wave propagation and the surface current remains reactive, forming circles around magnetic fields.

At a frequency of 3.3 GHz, the TE_{01} mode start to propagate, visible in Figure 5.29c. A large proportion of the current now reaches the output ports, providing output power, which is in-phase as opposed to the previous case. The propagation occurs due to the alignment of the current loop with the magnetic field lines in longitudinal direction, which leads to power transfer according to Equations (3.40a) and (3.40b). The output power increases sharply, as demonstrated in Figure 5.30.

change jsurf name in legend to surface current

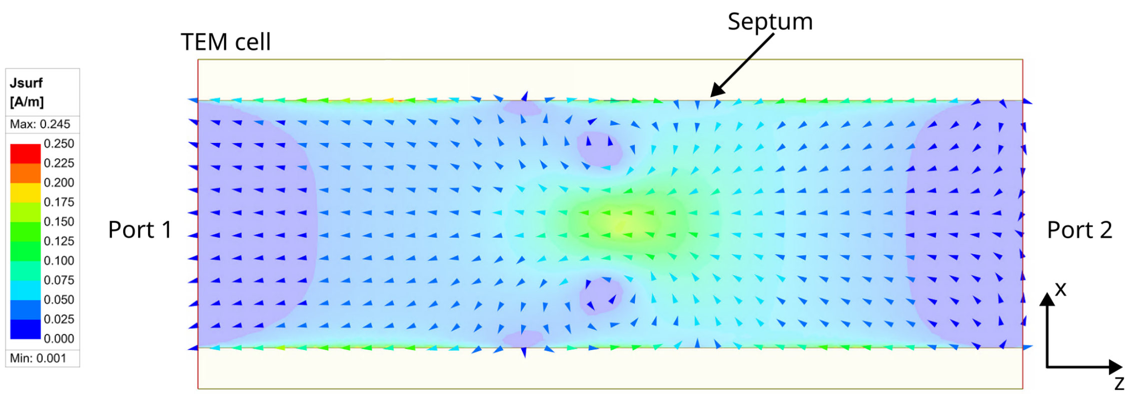

(a) Surface current density of septum induced by loop antenna at 3 GHz

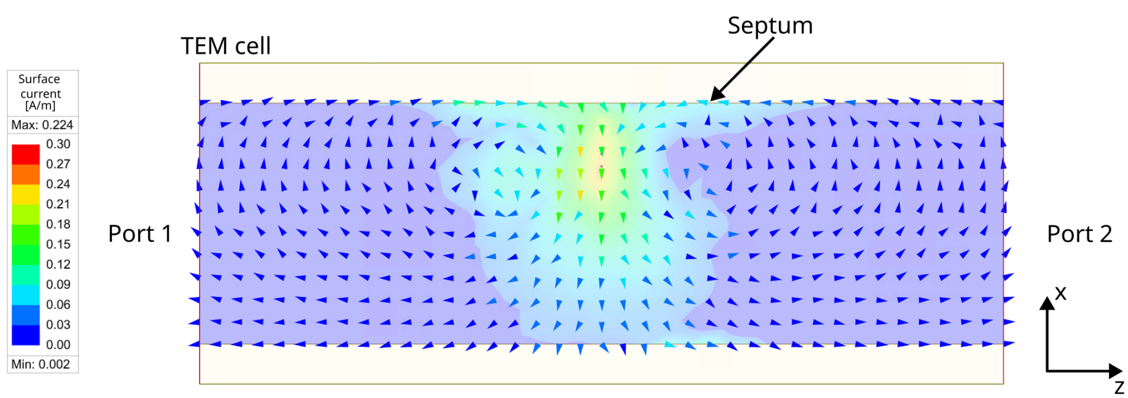

(b) Surface current density of loop antenna with offset of $x = 7\,\text{mm}$ and a 90 rotation angle at 100 MHz

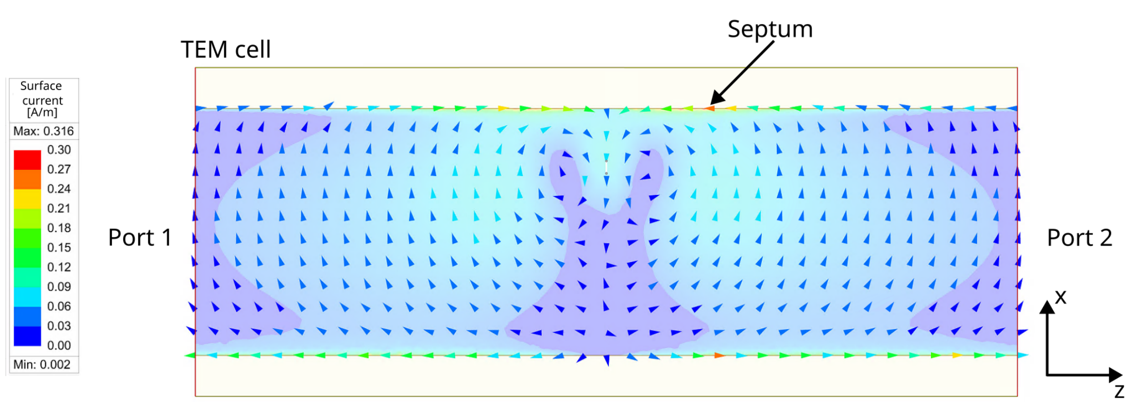

(c) Surface current density of loop antenna with offset of $x = 7\,\text{mm}$ and a 90 rotation angle at 3.3 GHz

Figure 5.29 Current surface densities at different frequencies, below and above the cut-off frequency of the TE_{01} mode.

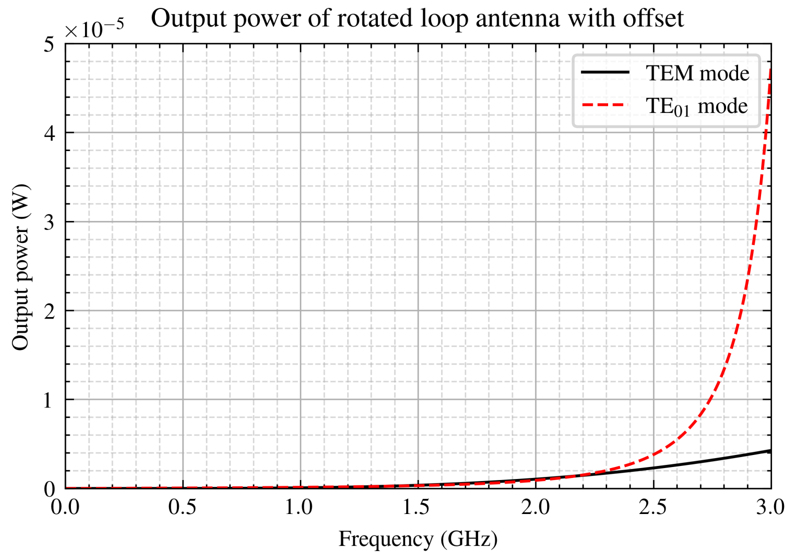

Figure 5.30 Output power transmitted by the antenna to an output ports through the TEM and TE_{01} separately over frequency. TODO: log scale, bigger frequency range

5.3.6 Influence of antenna's geometry

The antenna's geometry influences the coupling behavior. To demonstrate this, the loop antennas presented in are simulated, and their dipole moments and power consumption compared.

The behavior of the magnetic dipole moments $\mathbf{m}_m$ are equal in all cases according to Equations (3.40a) to (3.40b), since the total area of the loop antenna remains the same. Non-linearities persist, due to almost unchanging capacitance of the antenna to the upper PEC plane, causing increasing displacement current over frequency.

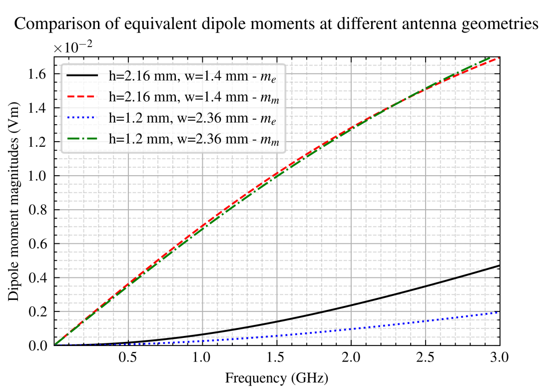

(a)

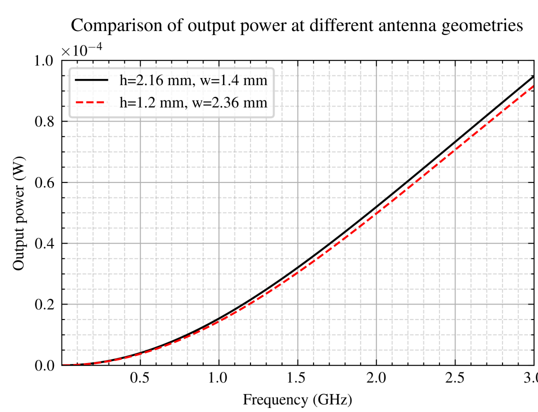

(b)

Figure 5.31 Dipole moments and phase shift of loop antenna

The electric dipole moment $\mathbf{m}_e$ is strongly influenced by the antenna's height. An antenna with large h leads to increased displacement currents to the septum.

5.4 Loop antenna with gap

5.4.1 Setup and geometrical analysis

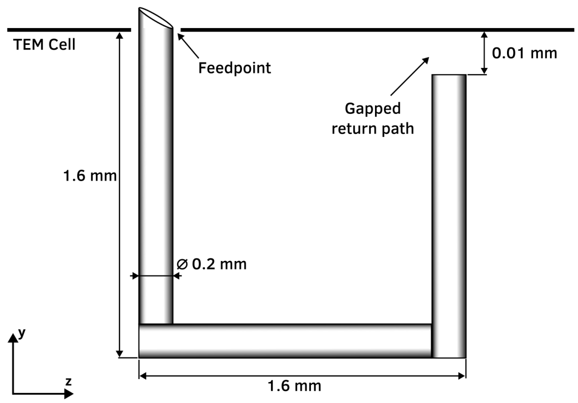

Figure 5.32 Geometry of loop antenna with a gap in the return path inserted in the TEM cell.

The geometry of the loop antenna with a gap is similar to that of the loop antenna discussed in subsection 5.3. A gap is present with 10 μm height in the return path, as shown in Figure 5.32. The magnetic coupling is determined with Equations (3.40a) to (3.40b), leading to

$$-\oint_C \boldsymbol{\tau} I(l) \cdot \mathbf{e}_n^{\pm} dl = -\int_{\text{wire}} \boldsymbol{\tau} I_{\text{wire}}(l) \cdot \mathbf{e}_n^{\pm} dl - \int_{\text{gap}} \boldsymbol{\tau} I_{\text{gap}}(l) \cdot \mathbf{e}_n^{\pm} dl. \tag{5.15}$$

The electric current in the gap is $I_{\text{gap}} = 0\,\text{A}$, while the current in the antenna wire I_{wire} is significantly reduced due to the interrupted current path. Consequently, the magnetic coupling between the loop antenna with a gap and the TEM cell is expected to be lower than that of the loop antenna without a gap.

The conductors around the gap act as capacitors, accumulating charges on both sides. This leads to a higher potential in the wire of the antenna. The electric coupling increases significantly, according to Equations (3.46a) to (3.46b). Concluding, the structure of the loop antenna with the gap suggests capacitive behavior with a dominating electric dipole moment.

TODO: Some sources state that electrically small antennas must be either strongly capacitive or inductive. This would mean, that small antennas can always be represented by the same model: Either dominating electric dipole moment in the capacitive antenna case, with a non-linear behavior of the high frequencies, or a magnetic dipole moment with the same property in the inductive antenna case. The frequency, at which the non-linearities occur, depend on the amount of capacitance or inductance, i.e. the Q-factor. A high Q-factor leads to non-linearities in lower cut-off frequencies, and a low Q-factor increases the cut-off frequency. A capacitive antenna with low impedance has a high Q-factor. A inductive antenna with high impedance has a high Q-factor. This can practically be read from the impedance graphs. Can a relation between the impedance/Q-factor and a "cut-off frequency" of the dipole moments be established?

TODO: A little thought experiment on the gapped loop antenna demonstrates why this is the case: If the magnetic dipole moment shall be increased in this antenna, the height of the gap can be decreased to increase the current flow and therefore the magnetic coupling. Ironically, this also increases the amount of charges accumulating on the boundaries of the gap, therefore increasing the electric coupling and capacitive behavior. The capacitive behavior can therefore not change, unless the gap is completely removed. Also, the decrease in gap leads to larger total energy transfer and a higher Q-factor. I suspect, that a high Q-factor of an antenna leads to high energy transfer. This would make sense, because a high Q-factor indicates increased near-field intensities, that would naturally couple with the tem cell. A simulation showing the dipole moments for different gap heights over the frequency would support this claim.

5.4.2 Equivalent dipole moments

The electric dipole moment shown in Figure 5.33a clearly dominates over the magnetic dipole moment. The dipole moments behave non-linearly over the frequency.

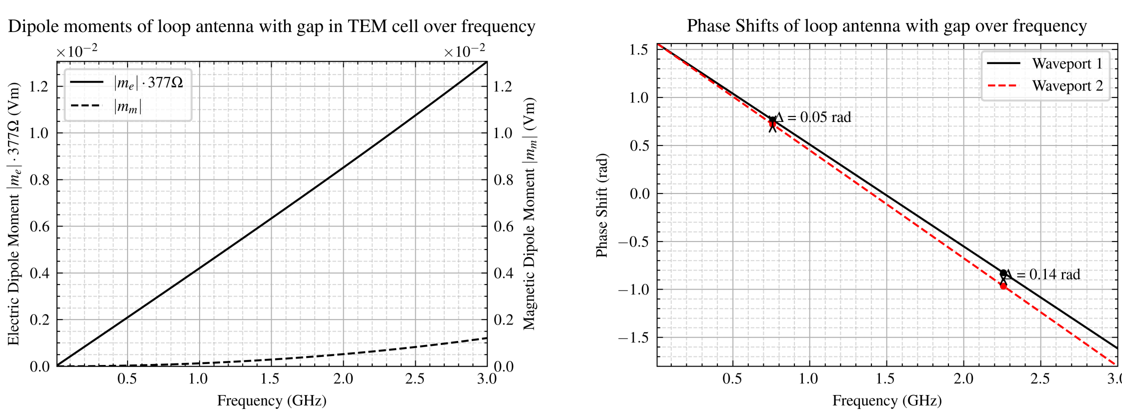

(a) (b)

Figure 5.33 Dipole moments and phase shift of loop antenna

Figure 5.34a demonstrates the effect of the gap height on the dipole moments' behavior.

A larger gap height leads to an decreased charge concentration in the gap region, consequently a smaller magnitude of the electric dipole moment $\mathbf{m}_\mathrm{e}$. Additionally, it also leads to a decrease in electric current $\mathbf{J}$ in the antenna, reducing the magnetic dipole moment $\mathbf{m}_\mathrm{m}$. The reduction in the magnitude of $\mathbf{m}_\mathrm{e}$ and $\mathbf{m}_\mathrm{m}$ with increasing gap height is reflected in the decreasing output power shown in Figure 5.34b.

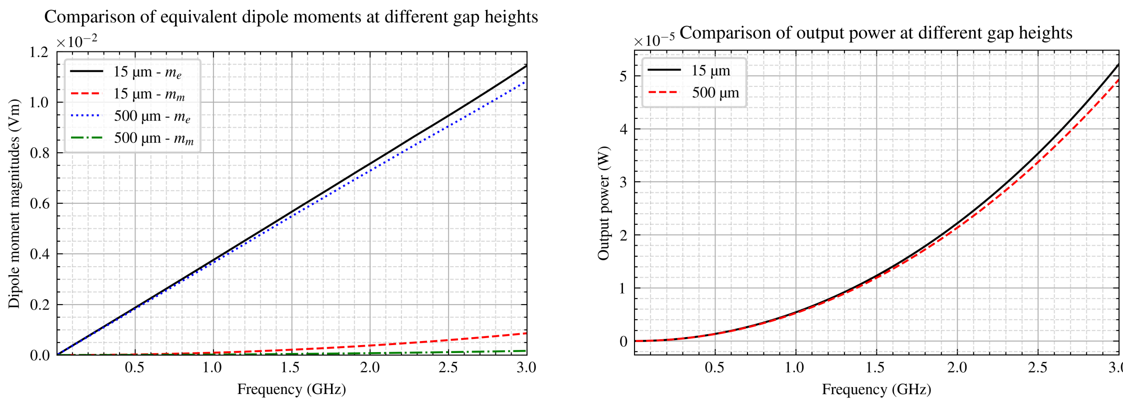

(a) **(b)**

Figure 5.34 Comparison of dipole moments and output power at different gap heights.

An increase in gap height reduces the non-linearities in $\mathbf{m}_\mathrm{e}$ and $\mathbf{m}_\mathrm{m}$. The voltage drop across the gap and the charge accumulation remains stabler over frequency. A small gap leads to both an increase in current and inductance, therefore creating a large voltage drop and influencing $\mathbf{m}_\mathrm{e}$ and $\mathbf{m}_\mathrm{m}$.

5.4.3 Electrical characteristics

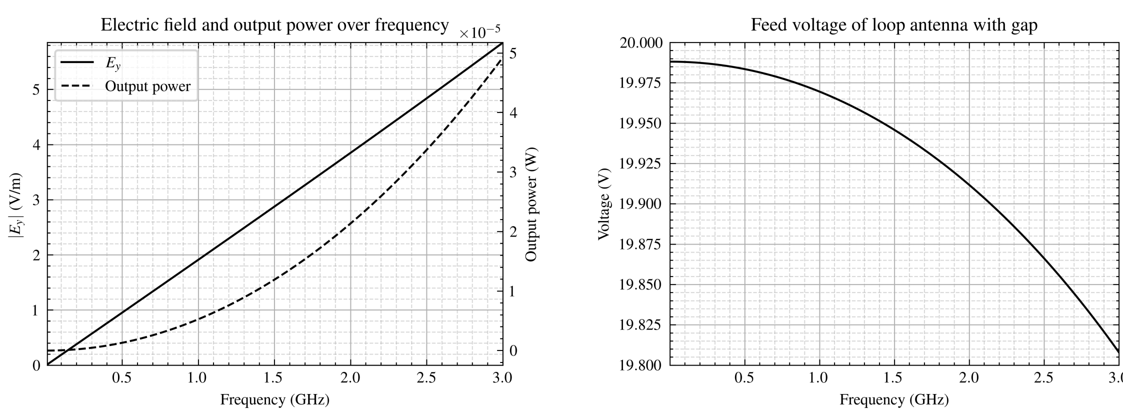

(a) Output electric field and power **(b)** Peak feed voltage

Figure 5.35 Electric field and power at the TEM cell's output port, and the peak feed voltage of the antenna.

The inductance of this antenna is not negligible, opposed to the case of the monopole antenna in subsection 5.2. This causes a significant magnitude of $\mathbf{m}_\mathrm{m}$ in Figure 5.33a and

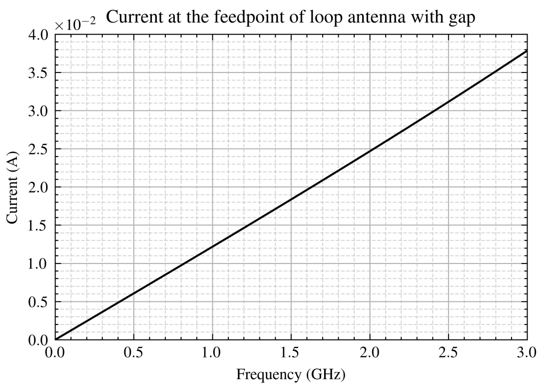

(a) RMS feed current.

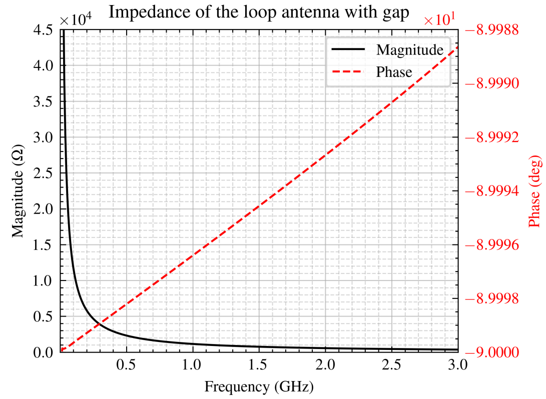

(b) Magnitude and phase of impedance

a stronger decline in impedance magnitude of the loop antenna with gap, shown in Figure 5.36b, compared to the monopole antenna's impedance, demonstrated in Figure 5.12b.

The gap leads to a significant reduction of electric current. Consequently, the impedance of the antenna shows capacitive behavior, as indicated in **??**. The energy transfer to the TEM cell occurs primarily by displacement current, explaining the dominating electric dipole moment due to Equation 3.47.

5.5 Inverted-F and center-fed monopole antenna

TODO

The inverted-F antenna (IFA) and center-fed monopole antenna are modeled in Ansys HFSS as shown in Figures 5.37a to 5.37b. Both have a maximum dimension of 5 mm and consequently are electrically small for a frequency of up to 6 GHz. They are both presented here, because of their similar geometry and electrical behavior. Both posses a current loop with equal area and a bar leading away from it. The bar of the CFM points towards the TEM cell's septum, and the bar of the IFA points towards an output port.

The center fed monopole antenna is shown in Figure 5.37a. The electric wire with the length of 5 mm points towards the septum.

A question on my mind since the beginning of this thesis: Can how is the magnetic dipole moment influenced by rotating this geometry by 90 degrees? Is the magnetic dipole moment higher or lower than in the rotated loop antenna? With my current knowledge, I suspect that the electric dipole moment leads to current coupling with the TEM cell over displacement current, therefore leading to a smaller magnetic dipole moment then in the case of the loop antenna

The loop area of the center-fed monopole antenna is equal to that of the loop antenna. Consequently, both antennas exhibit the same magnetic dipole moment.

CFM at 90° rotation still demonstrates magnetic dipole moment,

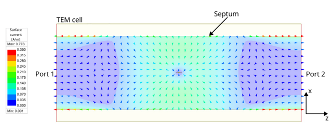

(a) Center-fed monopole antenna used in simulation

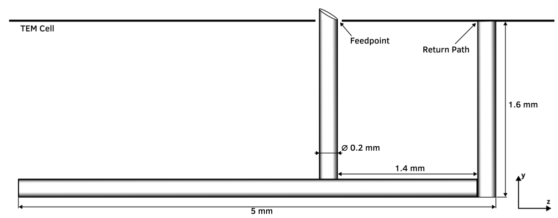

(b) Inverted F-antenna used in the simulation

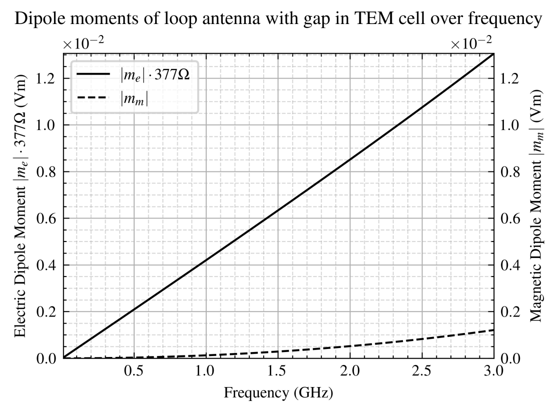

(c) PLACEHOLDER: Dipole moments comparison

Figure 5.37 Main figure caption with one subfigure on the left and two stacked on the right

6 Application of Shielding Techniques in TEM Cells

6.1 ASTM ES7-83 method

A model as described in subsubsection 3.5.1 is used to determine the shielding effectiveness of nickel and zink. The TEM cell contains a sheet of thickness ranging from 1 to 40 µm in the center at $z = 0$.

TODO: redo zinc simulation

Metallic thin shields are normally removed from the computational domain and replaced by impedance network boundary conditions on the surfaces of the shielding material [3]. Alternatively, the inside of the shielding material contains a fine mesh created with adaptive meshing, which is done here.

Material	Rel. permittivity ε_r	Rel. permeability μ_r	Conductivity σ
Zinc	≈ 1	≈ 1	1.67×10^7 S/m
Nickel	≈ 1	600	1.45×10^7 S/m

Table 6.1 Electromagnetic Properties of Zinc and Nickel

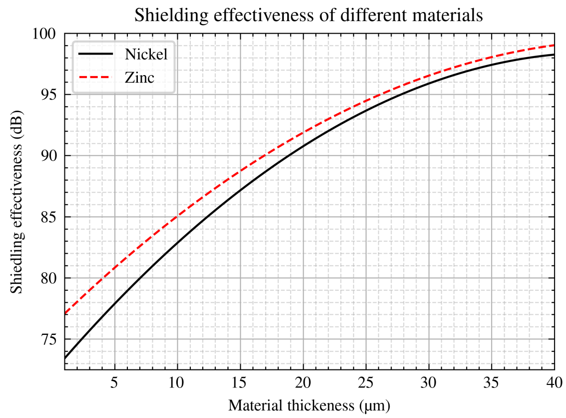

Figure 6.1 Shielding effectiveness of a sheet of zinc and nickel versus the material thickness.

6.2 Dual TEM cell

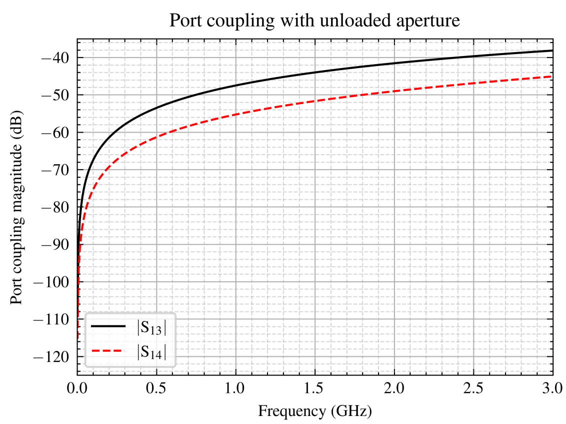

Figure 6.2 Coupling of port 1 to ports 3 and 4 with empty square aperture

Empty square aperture with side length of $d = 11.2\,\text{mm}$ used. Simulation model leans on measurement setup in [31].

6.3 Shielding Antennas

shielding antennas and investigating field distribution will be done here. Some tilt in shielding material would be interesting to investigate

6.4 Shielding Equivalent Dipole Moments

Check latex comments, which contain some good ideas. TODO Rest of section

References

[1] Constantine A. Balanis. *Advanced Engineering Electromagnetics*. John Wiley Sons, 2012.

[2] Constantine A. Balanis. *Antenna theory: Analysis and design. Buch Constantine A. Balanis*. 3rd. Wiley, 1997.

[3] C. Buccella et al. "Magnetic field computation in a physically large domain with thin metallic shields". In: *IEEE Transactions on Magnetics* 41.5 (2005), pp. 1708–1711. DOI: 10.1109/TMAG.2005.846059.

[4] Z. Cendes and D. Shenton. "Adaptive mesh refinement in the finite element computation of magnetic fields". In: *IEEE Transactions on Magnetics* 21.5 (1985), pp. 1811–1816. DOI: 10.1109/TMAG.1985.1063929.

[5] Z.J. Cendes. "Vector finite elements for electromagnetic field computation". In: *IEEE Transactions on Magnetics* 27.5 (1991), 3958–3966. DOI: 10.1109/20.104970.

[6] Z.J. Cendes and J.-F. Lee. "The transfinite element method for modeling MMIC devices". In: *1988., IEEE MTT-S International Microwave Symposium Digest* (1988), 623–626. DOI: 10.1109/mwsym.1988.22111.

[7] Robert E. Collin. *Field theory of guided waves*. IEEE Press, 2015.

[8] Saju Daniel and Sabu Thomas. "Shielding Efficiency Measuring Methods and Systems". In: *Advanced Materials for Electromagnetic Shielding: Fundamentals, Properties, and Applications*. 2019, pp. 61–87. DOI: 10.1002/9781119128625.ch4.

[9] David J. Griffiths. *Introduction to electrodynamics*. Cambridge University Press, 2024.

[10] Robert C. Hansen and Robert E. Collin. *Small antenna handbook*. Wiley, 2013.

[11] K.H. Huebner et al. *The Finite Element Method for Engineers*. A Wiley-Interscience publication. Wiley, 2001. ISBN: 9780471370789. URL: https://books.google.at/books?id=f3MZE1BYq3AC.

[12] John David Jackson. *Classical Electromagnetics*. 2nd ed. Wiley.

[13] J.P. Karst, C. Groh, and H. Garbe. "Calculable field generation using TEM cells applied to the calibration of a novel E-field probe". In: *IEEE Transactions on Electromagnetic Compatibility* 44.1 (2002), pp. 59–71. DOI: 10.1109/15.990711.

[14] M. Koch, C. Groh, and H. Garbe. "Exact Determination of Resonant Frequencies in TEM Cells". In: *13th International Zurich Symposium and Technical Exhibition on Electromagnetic Compatibility*. 1999, pp. 653–658. DOI: 10.23919/EMC.1999.10791592.

[15] Galen H Koepke. In: *Theory and measurements of radiated emissions using a TEM cell* (1989). DOI: 10.6028/nist.tn.1326.

[16] Dominik Kreindl et al. "A Simulation Workflow for Predicting IC Stripline Radiated Emissions of Bond Wire-Based Systems". In: *2024 14th International Workshop on the Electromagnetic Compatibility of Integrated Circuits (EMC Compo)*. 2024, pp. 69–73. DOI: 10.1109/EMCCompo61192.2024.10742020.

[17] Dominik Kreindl et al. "Evaluation of an analytical equivalent Hertzian dipole representation in tem cells applying the finite element method". In: *IEEE Transactions on Magnetics* 60.3 (2024), 1–4. DOI: 10.1109/tmag.2023.3324698.

[18] Dominik Kreindl et al. "Measurement and Simulation Methodology for Characterizing the Shielding Effectiveness of Coating Materials for Optical Sensors". In: *2023*

International Symposium on Electromagnetic Compatibility – EMC Europe. 2023, pp. 1–6. DOI: 10.1109/EMCEurope57790.2023.10274360.

[19] J.-F. Lee, D.-K. Sun, and Z.J. Cendes. "Full-wave analysis of dielectric waveguides using tangential vector finite elements". In: *IEEE Transactions on Microwave Theory and Techniques* 39.8 (1991), pp. 1262–1271. DOI: 10.1109/22.85399.

[20] J.F. Lee, D.K. Sun, and Z.J. Cendes. "Tangential vector finite elements for electromagnetic field computation". In: *IEEE Transactions on Magnetics* 27.5 (1991), pp. 4032–4035. DOI: 10.1109/20.104986.

[21] M.F.N. Mohsen. "Some details of the Galerkin Finite Element Method". In: *Applied Mathematical Modelling* 6.3 (1982), 165–170. DOI: 10.1016/0307-904x(82)90005-1.

[22] Cristian MORARI and Cristian BĂLAN. In: *Methods for determining shielding effectiveness of materials* (2015).

[23] D. Shenton and Z. Cendes. "Three-dimensional finite element mesh generation using Delaunay tesselation". In: *IEEE Transactions on Magnetics* 21.6 (1985), 2535–2538. DOI: 10.1109/tmag.1985.1064165.

[24] Ippalapalli Sreenivasiah, David Chang, and Mark Ma. "Emission characteristics of electrically small radiating sources from tests inside a tem cell". In: *IEEE Transactions on Electromagnetic Compatibility* EMC-23.3 (1981), 113–121. DOI: 10.1109/temc.1981.303930.

[25] GILBERT STRANG. *Analysis of the finite element method*. WELLESLEY-CAMBRIDGE Press, 2018.

[26] Son Xuat Ta, Ikmo Park, and Richard W. Ziolkowski. "Crossed Dipole Antennas: A review". In: *IEEE Antennas and Propagation Magazine* 57.5 (2015), pp. 107–122. DOI: 10.1109/MAP.2015.2470680.

[27] John C Tippet, David C Chang, and Myron L Crawford. In: *An analytical and experimental determination of the cutoff frequencies of higher-order te modes in a Tem cell* (1976). DOI: 10.6028/nbs.ir.76-841.

[28] C.M. Weil and L. Gruner. "High-order mode cutoff in rectangular striplines (short papers)". In: *IEEE Transactions on Microwave Theory and Techniques* 32.6 (1984), 638–641. DOI: 10.1109/tmtt.1984.1132745.

[29] Perry F Wilson. In: *Excitation of a tem cell by a vertical electric Hertzian dipole* (1981). DOI: 10.6028/nbs.tn.1037.

[30] Perry F. Wilson, David C. Chang, and Mark T. Ma. "Input Impedance of a Probe Antenna in a TEM Cell". In: *IEEE Transactions on Electromagnetic Compatibility* EMC-26.4 (1984), pp. 154–161. DOI: 10.1109/TEMC.1984.304216.

[31] Perry F. Wilson and Mark T. Ma. "Shielding-Effectiveness Measurements with a Dual TEM Cell". In: *IEEE Transactions on Electromagnetic Compatibility* EMC-27.3 (1985), pp. 137–142. DOI: 10.1109/TEMC.1985.304277.

[32] Perry F. Wilson and Mark T. Ma. "Simple approximate expressions for higher order mode cutoff and resonant frequencies in TEM cells". In: *IEEE Transactions on Electromagnetic Compatibility* 28.3 (1986), 125–130. DOI: 10.1109/temc.1986.4307269.